

**1Characterizing the Eemian-Weichselian transition in northwestern Europe with three multiproxy  
2speleothem archives from two Belgian cave systems (Han-sur-Lesse and Remouchamps).**

3Stef Vansteenberge<sup>1</sup>, Sophie Verheyden<sup>1</sup>, Dominique Genty<sup>2</sup>, Dominique Blamart<sup>2</sup>, Steven Goderis<sup>1</sup>, Stijn  
4J. M. Van Malderen<sup>3</sup>, Frank Vanhaecke<sup>3</sup>, Florent Hodel<sup>2</sup>, David Gillikin<sup>4</sup>, Camille Ek<sup>5</sup>, Yves Quinif<sup>6</sup>, Hai  
5Cheng<sup>7,8</sup>, R. Lawrence Edwards<sup>8</sup> and Philippe Claeys<sup>1</sup>

6Corresponding email: stef.vansteenberge@vub.be

7<sup>1</sup> Analytical, Environmental and Geochemistry, Vrije Universiteit Brussel, Pleinlaan 2, 1050 Brussels,  
8Belgium.

9<sup>2</sup> Laboratoire des Sciences du Climat et de l'Environnement, 91400 Gif-sur-Yvette, France

10<sup>3</sup> Atomic and Mass Spectrometry Group, Department of Analytical Chemistry, Universiteit Gent,  
11Krijgslaan 281 S12, 9000 Gent, Belgium.

12<sup>4</sup> Department of Geology, Union College, Schenectady, NY 12308, USA.

13<sup>5</sup> Université de Liège, 4000 Liège, Belgium.

14<sup>6</sup> Centre d'études et de Recherches Appliquées au Karst (CERAK), Faculté Polytechnique de Mons, 7000  
15Mons, Belgium.

16<sup>7</sup> Institute of Global Environmental Change, Xi'an Jiaotong University, Xi'an, China

17<sup>8</sup> Department of Earth Sciences, University of Minnesota, Minneapolis, USA.

18**Journal:** Quaternary Science Reviews

19**Abstract:**

20Interglacial to glacial transitions represent the most drastic turnovers in the Quaternary climate system.  
21Yet, millennial-scaled climate variability and stochastic internal variability that result in these transitions  
22remain still poorly understood. Here, three speleothem archives from two different cave systems in  
23Belgium (Han-sur-Lesse and Remouchamps) are investigated using a multiproxy approach in order to  
24characterize the last interglacial to glacial transition. The studied samples roughly span the period  
25between 125 ka and 100 ka, covering a large part of the Eemian and early Weichselian. The speleothems  
26show a high reproducibility for  $\delta^{13}\text{C}$ , which is interpreted as a proxy for past vegetation activity,  
27controlled by vegetation assembly above the cave. All three speleothems show a drastic increase in  $\delta^{13}\text{C}$   
28between 118 to 117 ka, reflecting a rapid change of vegetation assembly from last interglacial temperate  
29tree species towards glacial more open grass vegetation. This event shows a strong affinity in terms of  
30timing and climatic expression with the Late Eemian Aridity Pulse (LEAP) at  $118 \pm 1$  ka, identified in  
31pollen records from Western Germany. Aligning the chronologies of the two independently dated Han-

32sur-Lesse speleothem records enables a more precise absolute chronology and provides an age of  $117.7 \pm$   
330.5 ka to the start of this event in the Belgian speleothems. This event marks a distinct transition in the  
34Belgian speleothem proxies between Eemian optimum conditions and increased variability during the  
35glacial inception and the start of this event at  $117.7 \pm 0.5$  ka is therefore proposed as the Eemian-  
36Weichselian transition and consequently the start of the glacial inception in the studied speleothems.  
37High-resolution analysis shows that the  $117.7 \pm 0.5$  ka event is initiated by a cooling pulse followed by a  
38decrease in precipitation. A similar short-lived cooling event is also registered in multiple North-Atlantic  
39sediment archives. This study hypothesizes that the origin of the cooling event at 117.7 ka is an internal  
40climate response caused by the substantial amount of freshwater input from degraded ice-sheets by the  
41end of the Eemian (~120-118 ka). There is thus a clear climatic connection between the Belgian  
42speleothems and other continental European archives and North Atlantic marine archives, providing the  
43possibility of improving less constrained chronologies by alignment to the independently constructed  
44speleothem age-depth model presented in this study.

## 45Introduction

46 The study of past interglacial periods, in particular those considered to be (at least partially) warmer  
47than present, improves the understanding of the dynamics of the climate system within an anticipated  
48anthropogenic global warming forecasted for this century (Masson-Delmotte et al., 2013). The last  
49interglacial (LIG) experienced global average annual temperatures 1 to 2 °C higher than present (Otto-  
50Bliesner et al., 2013) and a global mean sea-level about 6 to 9 m higher than present (Dutton et al., 2015).  
51The LIG is so far the most intensively studied past interglacial. Using the definition of the Past  
52Interglacials Working Group of PAGES (Berger et al., 2016), interglacial periods are characterized by the  
53absence of Northern Hemisphere continental ice outside Greenland, resulting in a higher eustatic sea-level  
54compared to glacial periods. Based on such eustatic sea-level reconstructions the LIG period occurred  
55between 129 and 116 ka (Dutton and Lambeck, 2012; Govin et al., 2015). Subsequent to the LIG, the  
56glacial inception occurred which is defined as the transition from an interglacial climate state towards  
57colder, glacial climate conditions. However, it is not straightforward to assign absolute boundaries to this  
58complex sequence of events. This paper agrees with the reasoning presented by Berger et al. (2016) that  
59the end of the peak interglacial is considered as the initial stage of the subsequent glaciation, and thus the  
60glacial inception, despite the saw tooth pattern of recent ice age cycles. Additionally, the view advocated  
61by Govin et al. (2015) is followed, i.e. that the glacial inception lasts until the onset of Greenland Stadial  
6225 (GS-25) at 110.640 ka (GICC05modelext age, Rasmussen et al., 2014).

63 The last interglacial has been identified in numerous types of paleoclimate archives, including ice  
64cores of Greenland (NGRIP members, 2004; Neem Community, 2013) and Antarctica (Jouzel et al., 2007;  
65Capron et al., 2014 and references therein), marine sediment cores (Shackleton, 1969; Shackleton et al.,  
662003; Sanchez Goñi et al., 1999; Galaasen et al., 2014; Irvali et al., 2016), continental lake cores and/or  
67peat bogs (Woillard, 1978; Tzedakis et al., 2003; Sirocko et al., 2005; Brauer et al., 2007; Helmens, 2014)  
68and in speleothems (Drysdales et al., 2005; 2007; 2009; Meyer et al., 2008; Moseley et al., 2015;  
69Vansteenberghe et al., 2016; Regattieri et al., 2016; Demény et al., 2017). As a consequence, definitions of  
70the term ‘last interglacial’ can vary across studies (Kukla et al., 2002; Govin et al., 2015; Otvos et al.,  
712015). The continental LIG acme, which is the equivalent of Marine Isotope Stage 5e (MIS 5e,  
72Shackleton, 1969), is known as the Eemian. Although the Eemian was originally defined on a highstand  
73sequence in the Netherlands containing warm water mollusks (Otvos, 2015 and references therein),  
74nowadays it is mostly interpreted as an interval of warmer climate associated with the spread of temperate  
75mixed forests in areas covered by similar vegetation today (Woillard, 1978; Sanchez Goñi et al., 1999;  
76Kukla et al., 2002; Tzedakis et al., 2003). The Eemian is a diachronous unit, with longer durations in  
77southern Europe (127 to 109 ka; Müller and Sanchez Goñi, 2007) compared to northern Europe (~126 to  
78115 ka; Otvos, 2015). In the European continental terminology, the last glacial is defined as the  
79Weichselian. Consequently, the last glacial inception in continental records starts at the Eemian-  
80Weichselian transition (EWT) and lasts until the start of the continental equivalent of GS-25, which is the  
81Mélissy I (Woillard, 1978). Despite the extensive availability of last interglacial datasets, issues remain  
82unsolved, such as the underrepresentation of continental paleoclimate reconstructions (Tzedakis et al.,  
832015). Also, mechanisms, including millennial-scaled climate variability and stochastic internal  
84variability, that result in interglacial-glacial transitions (and vice-versa) remain still poorly understood  
85(Berger et al., 2016). Govin et al. (2015) recognized the strength of speleothems’ independent U-Th  
86chronology for alignment with other archives such as ice cores, pollen records and marine sediment cores.  
87To resolve the above mentioned questions, a multiple speleothem dataset from northwestern Europe  
88(Belgium) covering the Eemian and early Weichselian, thus including the last glacial inception, is  
89presented in this study. The dataset almost continuously covers the period between ca. 126 and 100 ka.  
90The use of multiple proxies, including growth rate, stable isotopes and trace elements, enables to translate  
91the geochemical signals observed in the samples in terms of paleoclimate changes in northwestern  
92Europe.

### 931. Background and earlier work

94 Speleothems have proven to be excellent recorders of regional, past continental climate change  
95(Fairchild et al., 2012). Their strength lies in the ability to construct accurate and independent

96chronologies using U-Th radiometric dating combined with speleothem specific age-depth modeling  
97algorithms (e.g. Scholz and Hoffmann, 2011; Breitenbach et al., 2012). Speleothem records from Europe  
98covering the Eemian and early Weichselian have provided detailed paleoclimate reconstructions (Genty et  
99al., 2013). However, the majority of these records are located in the Mediterranean realm or the Alps,  
100leaving large parts of northern Europe undocumented from a speleothem approach. An earlier study by  
101Vansteenberghe et al. (2016) has confirmed the potential of a Belgian speleothem and its variations in  
102carbon and oxygen stable isotope ratio proxies ( $\delta^{13}\text{C}$  and  $\delta^{18}\text{O}$ ) to reconstruct climate changes over the  
103Eemian to early Weichselian, expanding towards the northwest the spatial coverage of LIG European  
104speleothem records. This study relied on the speleothem named 'Han-9' (Fig. 2), which started growing at  
105 $125.3 \pm 0.6$  ka and consists of three growth phases. The first hiatus occurs between  $117.3 \pm 0.5$  ka and  
106 $112.9 \pm 0.4$  ka and a second hiatus starts at  $106.6 \pm 0.3$  ka. Unfortunately, there is poor age control on the  
107third and last growth phase, roughly lasting from  $\sim 103$  to  $\sim 97$  ka.  $\delta^{13}\text{C}$  and  $\delta^{18}\text{O}$  of the deposited  
108speleothem  $\text{CaCO}_3$  are presumed to be in equilibrium with the cave drip water. The amount of biogenic  
109 $\text{CO}_2$  within the soil above the cave, which depends on the type of vegetation above the cave, was  
110interpreted to control changes in speleothem  $\delta^{13}\text{C}$ . More depleted speleothem  $\delta^{13}\text{C}$  reflects more active  
111soils, resulting from a vegetation cover dominated by temperate trees while more enriched speleothem  
112 $\delta^{13}\text{C}$  reflects lower activity due to an increased presence of grass and shrub vegetation types. Speleothem  
113 $\delta^{18}\text{O}$  variations are controlled by a mix of local (e.g. temperature, precipitation) processes and more  
114regional effects (e.g. ocean source  $\delta^{18}\text{O}$ ). Stable isotope time-series revealed that Eemian optimum climate  
115conditions were present from (at least)  $125.3 \pm 0.6$  ka. Yet, between  $117.5 \pm 0.5$  ka and  $117.3 \pm 0.5$  ka, a  
116severe increase in  $\delta^{13}\text{C}$  (approximately 4 ‰) evidences a rapid change in vegetation assembly above the  
117cave. This change in vegetation occurs simultaneously as the Late Eemian Aridity Pulse (LEAP), a short-  
118lasting ( $\sim 0.4$  ka) dry event at  $118 \pm 1$  ka described by Sirocko et al. (2005) in the ELSA vegetation record,  
119constructed with pollen records from Eifel maar sediments (Germany). Therefore, the observed changes  
120in Han-9  $\delta^{13}\text{C}$  are interpreted to represent the same climate event as the LEAP in the ELSA vegetation  
121record. A similar climatic excursion was described from high-resolution marine records from the North  
122Atlantic: 1) a decrease in North Atlantic Deep Water (NADW) formation at 116.8 ka (Galaassen et al.,  
1232014) and 2) a drop in sea surface temperature with a simultaneous increase in ice rafted debris,  
124suggesting Greenland ice-sheet growth, dated at 117 ka (Irvali et al., 2014; 2016). The presence of these  
125events in the North Atlantic realm suggests a more global signature of this event than previously assumed.  
126In this perspective, Han-9 provided the first independent chronology for the event, i.e.  $117.5 \pm 0.5$  ka,  
127occurring right at the time where the glacial inception is expected in northwestern Europe. Han-9 stopped  
128growing during or shortly after the event making it impossible to place this event within the context of the  
129last glacial inception.

130 This study expands the last interglacial to early glacial Belgian speleothem dataset (Han-9) with  
131two additional speleothem records, one from the same cave and another from a second cave ~20 km  
132away. This additional dataset allows to test whether the observed changes in the Han-9 proxies are  
133reproducible in other speleothems on a regional scale and thus induced by regional paleoclimate changes.  
134Additionally, implementing a sample of a completely other deposition dynamics (massive speleothem vs  
135candle-shaped speleothem) from a second Belgian cave system (Remouchamps Cave) allows exclusion of  
136any cave specific effects altering the regional paleoclimate signal. These two new speleothem samples are  
137investigated through a multiproxy approach, using not only traditional stable isotope ratio time-series  
138( $\delta^{13}\text{C}$  and  $\delta^{18}\text{O}$ ) but also trace element time-series of magnesium (Mg), strontium (Sr), barium (Ba), zinc  
139(Zn), uranium (U), phosphorous (P), iron (Fe) and lead (Pb). By doing so, this study aims firstly to  
140improve the chronology regarding the timing and duration of the  $117.5 \pm 0.5$  ka event and secondly to  
141better understand the relation of this climate event to the Eemian-Weichselian transition (EWT) and the  
142last glacial inception.

## 1432. Study sites and speleothem samples

144 This study combines the results of three speleothem samples from two different cave systems (Han-  
145sur-Lesse Cave system,  $n = 2$ , and Remouchamps Cave,  $n = 1$ ) in Belgium. Both caves are located within  
146the *Calestienne*, a SW-NE trending superficial limestone belt of Middle Devonian age (Fig. 1C). After  
147deposition, these Paleozoic sediments underwent Hercynian folding followed by erosion in the Mesozoic.  
148The current hydrographic network was established from the Neogene to Pleistocene, by erosion into these  
149folded belts (Quinif, 2006). The caves are located ca. 200 km inland at an elevation of 200 m above sea  
150level for Han-sur-Lesse Cave system and 150-200 m above sea level for Remouchamps Cave,  
151respectively. Following the Köppen-Geiger classification (Peel et al., 2007), the climate in southern  
152Belgium is maritime with cool summers and mild winters. For the period 1999-2013, average year-  
153temperature was  $10.2^\circ\text{C}$  and average yearly rainfall amount  $820\text{ mm yr}^{-1}$ . This rainfall is spread over the  
154entire year with no distinct seasonal distribution (Royal Meteorological Institute, RMI).

### 1552.1 Han-sur-Lesse Cave system

156 To complement the work of Vansteenberge et al. (2016), one additional stalagmite sample was  
157retrieved from Han-sur-Lesse Cave: Han-8. The Han-sur-Lesse Cave system (Fig. 1B) is the largest  
158known subterranean karst network in Belgium, with a total length of ~10 km. The cave system was  
159formed by a meander cutoff of the Lesse River within the *Massif de Boine*, which is part of an anticline  
160structure consisting out of Middle to Late Givetian reefal limestones. The thickness of the epikarst zone  
161above the cave system is estimated to be around 40-70 m (Quinif, 2006). The area above the cave consists

out of C3 type vegetation with mainly temperate *Corylus*, *Fagus* and *Quercus* trees. As a natural reserve it has been protected from direct human influence for over 50 years (Timperman, 1989). The Lesse River enters the cave system at the *Gouffre de Belvaux* and exits at the *Trou de Han* approximately 24 hours later (Bonniver, 2010). Similar to Han-9, Han-8 was retrieved from the Southern Network, which is the most distal part of the cave system (Fig. 1B). Both stalagmites are candle shaped, with a length of 178 and 675 mm, respectively (Fig. 2). The Han-sur-Lesse Cave system is partly exploited as a show cave, but the Southern Network is not accessible for tourists. The Han-sur-Lesse Cave system consists of the Han-sur Lesse Cave and the Père Noël Cave and both have been intensively studied in the last three decades, making it the best understood cave system in Belgium. This includes speleothem dating and pollen analysis (Quinif and Bastin, 1994; Quinif, 2006), detailed hydrographic studies (Bonniver et al., 2010) and extended cave monitoring surveys (Genty and Deflandre, 1998; Verheyden et al., 2008; Van Rampelbergh et al., 2014), leading to successful paleoclimate reconstructions on Holocene speleothems down to seasonal scale (Verheyden et al., 2000; 2006; 2012; 2014; Van Rampelbergh et al., 2015, Allan et al. 2015).

### 3.2 Remouchamps Cave

An additional stalagmite core sample, RSM-17 (Fig. 2), was retrieved from Remouchamps Cave in 2012. This cave is located ~100 km southeast of Brussels, on the eastern bank of the Amblève River (Fig. 1D). The elongated cave is formed along inverse faults within biostrome limestone deposits of Middle Frasnian age (Ek, 1970; Coen, 1970). The cave consists of an upper (Fig. 1D in black) and a lower level (Fig. 1D in grey) and has a total length of ~3.9 km. The subterranean river Rubicon flows through the lower level of the cave. The area above the cave consists of similar C3 type deciduous forest vegetation as Han-sur-Lesse Cave. RSM-17 stalagmite is an approximately 3 m large, fallen and broken stalagmite located within the *Salle des Ruines*. RSM-17 was among the first speleothems in Belgium to be dated using U-Th (Gewelt, 1985). In this study, RSM-17 is represented by 2 cores that were taken from the speleothem (Fig. 2). Core 1 was drilled from the base of the speleothem towards the top and is 1303 mm long. However, the upper part of core 1 (starting at 371 mm dft) missed the speleothem's central growth axis therefore a second core was taken from the top of the speleothem towards the bottom. The 2 cores were aligned based on the presence of a distinct, dense and brown layer, as shown by the black line in Fig. 2.

## 13. Methods

### 14.1 U-Th dating and age-depth modeling

193 To construct robust age-depth models, 35 samples are taken along the three speleothems' growth axis  
 194 for radiometric dating (see Fig. 2 for locations). This includes 13 samples of Han-8 and 17 samples of  
 195 RSM-17. Five additional samples (marked in green on Fig. 2) are taken from Han-9 to improve the  
 196 existing age-depth model, which was originally constructed with 23 dates (Vansteenberghe et al., 2016).  
 197 All ages are acquired by U-Th dating at the University of Minnesota Earth Sciences Department  
 198 (Minneapolis, USA). For all U-Th analyses, 150-300 mg of speleothem calcite is milled and analyzed  
 199 with a Neptune multiple-collector plasma source mass spectrometer (MC-ICP-MS, Thermo-Fisher  
 200 Scientific, Bremen, Germany). Ages are corrected assuming an initial  $^{230}\text{Th}/^{232}\text{Th}$  atomic ratio of  $4.4 \pm 2.2$   
 201  $\times 10^{-6}$ . The age datum is 1950 CE. For additional information about the applied method, see Edwards et  
 202 al. (1987), Shen et al. (2012) and Cheng et al. (2013) and references therein. Age-depth modeling is done  
 203 using the StalAge algorithm (Scholz and Hoffmann, 2011; Scholz et al., 2012) in R (R Core Team, 2013).  
 204 Depths are expressed as distance from top (dft) in mm. The outcome of the StalAge algorithm is a final  
 205 age-depth model that is the median of the simulated fits with a  $2\sigma$  error, which is calculated through the  
 206 distribution of the simulated fits (Scholz and Hoffmann, 2011). One of the key advantages of the StalAge  
 207 algorithm is that it does not have any adjustable parameters, enabling a high-degree of reproducibility.  
 208 The only choice a user can make is whether outlier dates should be disregarded in the modeling process  
 209 or if their corresponding errors should be increased in order to fit the model. A disadvantage, however, is  
 210 that the model does not handle substantial changes in growth rate in the boundary areas of the  
 211 speleothem, i.e. top and base, very well (Scholz and Hoffmann, 2011). The resulting age-depth model is  
 212 then used to calculate corresponding growth rates, expressed in  $\text{mm ka}^{-1}$ . Additionally, the chronology is  
 213 further improved by aligning the independent Han-8 and Han-9 age-depth models to each other by  
 214 selecting specific corresponding tie points in both speleothems'  $\delta^{13}\text{C}$  time-series.

#### 215 4.2 Stable isotope ratio ( $\delta^{13}\text{C}$ and $\delta^{18}\text{O}$ ) analysis

216 Speleothem subsamples for stable isotope ratio ( $\delta^{13}\text{C}$  and  $\delta^{18}\text{O}$ ) analysis are drilled along the  
 217 speleothems' growth axis (Fig. 2) using a MicroMill (Merchantek, Electro Scientific Industries Inc.,  
 218 Portland, USA), which is a computer steered drill mounted on a Leica GZ6 microscope (Leica  
 219 Microsystems GmbH, Wetzlar, Germany). The MicroMill system is equipped with tungsten carbide dental  
 220 drill bits 300 or 1000  $\mu\text{m}$  in diameter (Komet Dental, Lemgo, Germany). Samples were stored at  $50^\circ\text{C}$   
 221 prior to analysis to avoid contamination. Sample locations are indicated in Fig. 2 and spatial resolution  
 222 varies as a function of the speleothems growth rate between 5 mm (RSM-17) and 250  $\mu\text{m}$  (Han-8). For  
 223 RSM-17 ( $n = 266$ ) and the high-resolution part of Han-8 (65-89.5 mm dft,  $n = 63$ , Fig. 2),  $\delta^{13}\text{C}$  and  $\delta^{18}\text{O}$   
 224 measurements are done at the Stable Isotope Laboratory, Vrije Universiteit Brussel (Brussels, Belgium)  
 225 using a Perspective isotopic ratio mass spectrometer (IRMS) coupled to a Nucarb automated carbonate

226preparation system (Nu Instruments, Wrexham, UK). The Nu Instruments setup makes use of an in-house  
227standard MAR-2(2), made from Marbella limestone and which is calibrated against the international  
228standard NBS-19 (Friedman et al., 1982). Reported values for the MAR-2(2) standard are 3.41 ‰ Vienna  
229Pee Dee Belemnite (VPDB) for  $\delta^{13}\text{C}$  and 0.13 ‰ VPDB for  $\delta^{18}\text{O}$ . Averages of the total 2 $\sigma$  uncertainties  
230for  $\delta^{13}\text{C}$  and  $\delta^{18}\text{O}$  are 0.03 ‰ and 0.08 ‰ for the Nu Perspective setup. Other Han-8 stable isotope ratios  
231( $n = 162$ ) are measured on a VG Optima dual-inlet IRMS (Thermo-Fisher Scientific, Bremen, Germany)  
232at the Laboratoire des Sciences du Climat et de l'Environnement (Gif sur Yvette, France). NBS-19 was  
233used as a reference material (Friedman et al., 1982). Analytical errors are 0.05 ‰ and 0.08 ‰ for  $\delta^{13}\text{C}$  and  
234 $\delta^{18}\text{O}$ , respectively. At regular intervals, a replicate sample was measured in a different batch to check for  
235the reproducibility of the analytical method.

### 2363.1 Trace elements

237 Two methods for speleothem trace element analysis are applied in this study. The Han-8 trace  
238element record (Fig. 2), consisting of Mg, Al, P, Zn, Sr, Ba, Pb, and U, is constructed using laser ablation  
239inductively coupled plasma mass spectrometry (LA-ICP-MS) at the Royal Africa Museum (Tervuren,  
240Belgium). A Fisons-VG frequency quadrupled Nd-213 YAG laser ( $\lambda = 266$  nm) coupled to a Fisons-VG  
241214 PlasmaQuad II+ mass spectrometer is used. Data are calibrated using both the NIST 610 (Pearce et  
242al., 1997) and the USGS MACS1. Calibration (including blank subtraction and drift correction) is  
243performed offline by using Ca as internal reference. Details of LA-ICP-MS operating conditions can be  
244found in Lazareth et al. (2003). A total of 3702 data points are collected on Han-8 speleothem with an  
245average spatial resolution of  $\sim 40$   $\mu\text{m}$ . Errors are calculated using the relative standard deviation (RSD) of  
246NIST 610.

247 Trace elements for RSM-17 were only collected on a specific 76.56 mm long transect that covers the  
248Eemian-Weichselian transition, i.e. between 596 and 518 mm dft (Fig. 2). RSM-17 trace element  
249concentrations are determined using inductively coupled plasma mass spectrometry complemented by a  
250LA-ICP-MS at the Atomic and Mass Spectrometry Group, Ghent University (Ghent, Belgium). The LA-  
251ICP-MS setup consists of a 193 nm ArF\*excimer Analyte G2 laser ablation system (Teledyne Photon  
252Machines, Bozeman, MT, USA) coupled to a single-collector sector field Element XR ICP-MS unit  
253(Thermo Fisher Scientific, Bremen, Germany). The laser is used to sample adjacent positions along a line  
254segment parallel to the stalagmite's growth axis. The positions are ablated one-by-one for 15 s with a laser  
255spot size 110  $\mu\text{m}$  in diameter. A total of 696 positions are sampled. Sampling via individual drilling points  
256is preferred here over the conventional approach of continuous line scanning because the single positions



can be sampled longer, resulting in an improved limit of detection for low concentration elements, for example Y.

## 4. Results

The results of U-Th dating are presented in Table 1. Errors represent a  $2\sigma$  uncertainty. The speleothem samples from both cave sites have a comparable  $^{238}\text{U}$  content, with an average of  $284 \text{ ng g}^{-1}$  (SD =  $105 \text{ ng g}^{-1}$ ) for the Han-sur-Lesse samples and  $250 \text{ ng g}^{-1}$  (SD =  $97 \text{ ng g}^{-1}$ ) for the Remouchamps samples. In general, detrital Th contamination is low, with average  $^{230}\text{Th}/^{232}\text{Th}$  atomic ratios of  $11732 \times 10^{-6}$  and  $4217 \times 10^{-6}$  for Han-sur-Lesse speleothems and RSM-17, respectively. The resulting ages are plotted in Fig. 3, with previously published ages of Han-9 (Vansteenberghe et al., 2016) marked in red. The new date obtained at the end of the first Han-9 growth phase, date 1, is consistent with the previously obtained age model. For growth phase 2, date 2 is not in stratigraphic agreement with earlier obtained ages. In the third growth phase, date 4 and 5 appear to be more consistent with the earlier obtained older dates, i.e. the batch that was dated in 2013 (Vansteenberghe et al., 2016), instead of the younger ages (the batch that was dated in 2015, marked with an \* in Table 1). For Han-8, all determined ages are stratigraphically consistent, i.e. no age inversions occur. Errors range between 0.5 ka ( $\sim 0.4\%$ ) and 0.368 ka ( $\sim 0.3\%$ ). In contrast to the stratigraphically consistent data of Han-8, the age-depth plot of RSM-17 shows increased scattering from date 3 to 10 (i.e. between 1100 and 670 mm dft, Fig. 3). Yet, the  $^{238}\text{U}$  content and  $^{230}\text{Th}/^{232}\text{Th}$  atomic ratios are not significantly different from the other dates (Table 1).

Figure 5 shows the results of the stable isotope and trace element analysis of Han-8 and RSM-17 together with previously obtained  $\delta^{13}\text{C}$  and  $\delta^{18}\text{O}$  of Han-9 (Vansteenberghe et al., 2016).  $\delta^{13}\text{C}$  values of RSM-17 are the most negative of all three speleothem  $\delta^{13}\text{C}$  records with an average of  $-10.92\text{‰}$  and a standard deviation of  $0.70\text{‰}$ . Han-8  $\delta^{13}\text{C}$  varies between  $-3.45$  and  $-7.58\text{‰}$  with an average of  $-5.87\text{‰}$  and a standard deviation of  $1.16\text{‰}$ . Starting from the base of the speleothem ( $\sim 122$  ka) up until  $\sim 117.7$  ka,  $\delta^{13}\text{C}$  varies roughly between  $-6$  and  $-7.5\text{‰}$ , except for a positive excursion to  $-4.98\text{‰}$  at  $121.5$  ka. The amplitude of  $\delta^{13}\text{C}$  variations after  $117.7$  ka, which is about  $4\text{‰}$ , is much larger compared to the bottom part of the stalagmite. Compared to  $\delta^{13}\text{C}$ , the range of  $\delta^{18}\text{O}$  fluctuations in RSM-17 and Han-8 is smaller. The  $\delta^{18}\text{O}$  signal of RSM-17 has an average of  $-5.00\text{‰}$  and a standard deviation  $0.41\text{‰}$ . Han-8  $\delta^{18}\text{O}$  values fluctuate between  $-4.92$  and  $-6.72\text{‰}$ , with an average and standard deviation of  $-5.81\text{‰}$  and  $0.35\text{‰}$ , respectively. Han-8 Mg, Sr, Ba and U trace element concentrations show a similar trend as Han-8  $\delta^{18}\text{O}$ , with little variation between  $122$  and  $115$  ka (except for an excursion around  $117.7 - 117$  ka) and lowest values from  $115$  to  $112$  ka. This trend is opposite for P, with highest concentrations between  $115$  and  $112$  ka.

Trace element distance series of RSM-17 are shown in Fig. 7. Thick layers, consisting of alternations between dense, dark calcite and white, porous calcite occur before 545 mm dft. After 545 mm, layers are significantly thinner. All elements display sinusoidal variations corresponding with the visible layering. Magnesium concentrations are higher after 545 mm dft and Sr and Ba variations are in antiphase with Mg and show a decrease after 545 mm dft. U behaves in a similar way as Sr and Ba, although the transition between higher and lower concentrations at 545 mm dft is more gradual. Aluminum and Zn have higher concentrations after 545 mm dft similar to Sr, Ba and U. Concentrations of P and Y are higher before 545 mm dft.

## 2975. Discussion

### 2995.1 Age-depth models

The age-depth models for the two new speleothems (Han-8 and RSM-17) and the improved model of Han-9 are shown in Fig. 3. The studied samples roughly span the period between 125 ka and 100 ka, with all three speleothems covering 121 ka to 117.5 ka and 113 ka to 111 ka. Although Han-9 and Han-8 were located just 0.5 m apart, their age-depth models are substantially different from each other. More specifically, Han-9 starts growing about 4 ka before Han-8 and shows much larger variations in growth rate, with two hiatuses occurring. The basal age of the RSM-17 core is 120 ka, however the base of the stalagmite was not sampled.

#### 307Han-9

The additional Han-9 ages provide the ability to improve the existing age-depth model. Han-9 displays intermittent growth with 3 growth phases (GP's) separated by two hiatuses (Fig. 3). GP 1 starts at  $125.3 \pm 0.6$  ka with stable growth rate of  $20 \text{ mm ka}^{-1}$ . After 121 ka, growth rate significantly increases to  $150 \text{ mm ka}^{-1}$ . Date 1 (Table 1, Fig. 3) confirms the high growth rate at the end of GP 1 from 121 ka to 117.3 ka. A first hiatus starts at  $117.3 +0.4/-0.8$  ka. Compared to the earlier model by Vansteenberge et al. (2016), date 1 reduces the error of the age-depth model on the start of the first hiatus, i.e. from  $117.3 +0.7/-1$  ka to  $117.3 +0.4/-0.8$  ka. The hiatus lasts  $4.5 +0.8/-1.2$  ka and at  $112.8 \pm 0.4$  ka the second growth phase starts. During this GP, growth rate remains at a constant pace of  $40 \text{ mm ka}^{-1}$  until approximately 110.5 ka, where it decreases to  $6 \text{ mm ka}^{-1}$ . Date 2 is considered as an outlier and was disregarded during the modeling algorithm. Date 3, taken at the end of the second growth phase, confirms the earlier hypothesis of severely decreased growth rate between  $\sim 110$  and  $\sim 106$  ka (Vansteenberge et al., 2016). At  $106.2 \pm 0.5$  ka, GP2 ends. The second hiatus lasts until  $103.8 +0.6/-0.5$  ka. The ages of GP 3 provided by Vansteenberge et al. (2016) contain several age inversions. The model presented here, with GP 3 between

321 103.8  $\pm$ 0.6/-0.5 ka and 99.7  $\pm$ 0.3 ka is based on the newly added dates in this study (date 4 and date 5).  
322 Four dates were considered as outliers and were not taken into account to construct the age model (Fig.  
323 3). The model now displays a slow growth at the start of GP3 at 103.8  $\pm$ 0.5 ka, followed by an increase in  
324 growth rate at  $\sim$ 100.8 ka. Given this age-depth model, stable isotopes were analyzed with a temporal  
325 resolution between 100 and 0.3 years, and an average of 16 years.

## 326 Han-8

327 All Han-8 dates are stratigraphically consistent, making the age-depth model robust and  
328 straightforward. Han-8 starts growing at 122.6  $\pm$ 0.6/-0.5 ka. Throughout its growth, a more or less  
329 constant growth rate of  $\sim$ 20 mm ka<sup>-1</sup> is maintained. A discontinuity in the speleothem, at 81.5 mm dft  
330 (Fig. 2), appears to represent a short hiatus that starts at 117.7  $\pm$ 0.4 ka and ends at 117.0  $\pm$ 0.3 ka.  
331 However, the duration of this hiatus is only slightly longer than the error of the age model. Han-8 stops  
332 growing at 111.9  $\pm$ 0.5 ka.

## 333 RSM-17

334 The U-Th ages of RSM-17 show scatter between 1100 and 670 mm dft, with several age inversions.  
335 Yet, this scatter is believed to be caused by extreme high growth rates, up to 240 mm ka<sup>-1</sup>, which is  
336 reflected in the presence of layers up to 1 mm thick. The layers are assumed to be annual since 1) the  
337 similarity of the dark-light layer couplets to those of actively growing annually layered speleothems  
338 (Verheyden et al 2006; Van Rangelbergh et al., 2014; 2015) in Han-sur-Lesse cave and 2) the sinusoidal  
339 variations of trace element proxies in one dark-light layer couplet which are similar to those observed in  
340 actively growing annually layered stalagmites (Fig. 7). Counting of these layers in between U-Th dates  
341 could not confirm nor did it reject the hypothesis of the annual nature of these layers. To construct the  
342 RSM-17 age-depth model shown in Fig. 3, date 4 and date 9 were considered as major outliers and  
343 removed during the StalAge age-depth modeling process. The final model shows that the bottom of the  
344 RSM-17 core is 120.0  $\pm$ 0.4 ka old. High growth rates ( $>$ 200 mm ka<sup>-1</sup>) are maintained until  $\sim$ 116.5 ka, with  
345 the exception of short decrease at  $\sim$ 118 ka. From 115 ka, growth rate lowers to 100 -120 mm ka<sup>-1</sup> which is  
346 maintained throughout the upper part of the core, dated at 112.7  $\pm$ 0.8/-0.9 ka.

## 347 5.2 Alignment of Han-9 and Han-8 age-depth models

348 To construct an even more precise chronology for the Eemian Weichselian transition and other  
349 climatic events during the last glacial inception, Han-8 and the adjusted Han-9 age-depth models are  
350 aligned to each other based on their  $\delta^{13}\text{C}$  record. Conventionally, in alignment strategies, one record is  
351 aligned to another reference record of which the chronology is well-established based on simultaneous

changes in a climate variable or proxy (Govin et al., 2015). In this case, both Han-8 and Han-9 have an independently constructed chronology. Therefore, it would be incorrect to select one sample as the reference record by assuming that this sample has the correct age-depth model. To avoid this, both age-depth models are aligned to each other and the average of both models is calculated, with both age-depth models contributing equally to the resulting model. The proxy used for aligning both records is  $\delta^{13}\text{C}$ . Variations in Han-9  $\delta^{13}\text{C}$  are interpreted to reflect changes in vegetation activity above the cave, resulting from changes in the type of vegetation cover (Vansteenberghe et al., 2016). Changes in vegetation activity should therefore result in a similar Han-8  $\delta^{13}\text{C}$  record, but only if there is no overprint of kinetic fractionation. Checking for kinetic fractionation by applying Hendy Tests (Hendy, 1971) is not feasible since individual layers cannot be identified due to the low growth rates of both stalagmites. However, the striking similarity between both Han 8 and 9  $\delta^{13}\text{C}$  isotopic profiles, even in terms of absolute values (Fig. 3634), is a strong argument for the absence of important kinetic effects that could have overprinted the vegetation signal. This Replication Test to evaluate the likelihood of calcite deposition under isotopic equilibrium is proposed by Dorale and Liu (2009) as a better alternative for the Hendy Test. Alignment of both records is carried out by arbitrarily selecting eight tie-points between 123 and 111 ka, as shown in Fig. 4, that are interpreted to represent a similar point in time. Next, the ages of these points are extracted from each of the two age-depth models and the average age is calculated (Table 2), after which a new age-depth model is constructed for both speleothems based on these average ages. The  $2\sigma$  uncertainty of the new age-depth model is calculated with the average of the upper and lower  $2\sigma$  values of the original age-depth models. Also, as shown in Table 2, the newly calculated age-depth model lies within the age uncertainty of the original Han-8 and Han-9 age-depth models. For example, the start of the first hiatus in Han-9 and the small hiatus in Han-8 occur at  $117.3 +0.4/-0.8$  ka and  $117.7 \pm 0.4$  ka, respectively. In the new aligned age-depth model, the start of both hiatuses is interpreted to occur at the same time, which is  $117.5 \pm 0.5$  ka. Other proxy time-series, such as  $\delta^{18}\text{O}$  and trace elements, are then constructed using this aligned age-depth model. The  $\delta^{13}\text{C}$  record of RSM-17 was not included in the alignment because of the higher uncertainties in the age-depth model.

### 5.3 Eemian acme between 125.3-117.5 ka

The terminology proposed by Govin et al. (2015) is followed in this study, i.e. the term ‘acme’ is used to represent the interval of peak values in climate or environmental record that is contained within the LIG. All three speleothems show the presence of Eemian  $\delta^{13}\text{C}$  acme conditions between 125.5 and 117.5 ka. This is indicated by the low  $\delta^{13}\text{C}$ , suggesting vegetation similar to that of today, i.e. dominated by temperate tree species, which reflects warm and moist conditions. The start of Han-9 speleothem growth

384 is interpreted to reflect the presence of relatively wetter conditions between 125 and 124 ka  
 385 (Vansteenberghe et al., 2016), as earlier identified in speleothems from southwest France (Couchoud et al.,  
 386 2009) and central Europe (Demény et al., 2017). Yet, the ELSA vegetation record (Eifel, Germany,  
 387 Sirocko et al., 2005) and speleothems from Corchia Cave (Italy, Drysdale et al., 2005) suggest the  
 388 presence of warm and moist last interglacial conditions before Han-9 starts growing at 125.3 ka. Which is  
 389 consistent with the very low Han-9  $\delta^{13}\text{C}$  of  $\sim 9\text{‰}$  at 125.3 ka. So far, Han-9 is the oldest known Last  
 390 Interglacial speleothem formation from Han-sur-Lesse and other caves in Belgium. Although older LIG  
 391 speleothems could be present (but have not been identified yet) it is hypothesized that an effective  
 392 precipitation increase at 125.5 was necessary besides the already present LIG acme to initiate speleothem  
 393 formation. This short period of wetter conditions, that initiated Han-9 growth, likely follows as what can  
 394 be described as a ‘mid-Eemian climate depression’, i.e. a short duration of colder and dryer conditions  
 395 occurring around 126–125 ka, which is reflected in European pollen records. For example, vegetation  
 396 reconstructions based on pollen from Lago Grande di Monticchio (Italy) indicate a drop in *Quercus* pollen  
 397 and a simultaneous increase in Graminae pollen at  $\sim 125$  ka, (Brauer et al., 2007), interpreted a short dry  
 398 interval. In addition, sediment archives from the North Atlantic (NEAP-18K: Chapman and Shackleton,  
 399 1999; ODP-980: Oppo et al., 2006; U1304: Hodell et al., 2009; MD03-2664: Galaasen et al., 2014; Irvali  
 400 et al., 2016) and the Norwegian Sea (Fronval et al., 1998) also showed the presence of a mid-Eemian  
 401 cooling. Global sea-level reconstructions even suggest the occurrence of a small regression at  $\sim 125$  ka  
 402 (Hearty et al., 2007, Fig. 8). In the Eifel (Germany), a decrease in *Pinus* and *Betula* pollen and an increase  
 403 in temperate tree pollen, e.g. *Quercus* and *Carpinus*, follows a short spike in grass pollen abundance at  
 404 125 ka (Fig. 8). This indicates a transition to warm and wetter conditions during the second part of the  
 405 Eemian, starting at  $\sim 124$  ka. At 122.1 ka, an increase in  $\delta^{13}\text{C}$  of  $+1.5\text{‰}$  in Han-8 and  $+1.2\text{‰}$  in Han-9,  
 406 respectively, occurs. This increase could potentially be correlated to an observed cold event at 122.3 ka in  
 407 the Norwegian Sea, expressed by near-glacial ocean surface summer temperatures (Bauch et al., 2011).  
 408 Additionally, Zhuravleva et al. (2017) identified an intermittent sea surface cooling in the Arctic region  
 409 triggered by a meltwater release at  $\sim 122$  ka. Overall, the observations from the Han-sur-Lesse  
 410 speleothems confirm earlier hypothesis that question the general view of stable Eemian optimum  
 411 conditions between 128 and 117 ka (Bauch et al., 2011; Irvali et al., 2012; Capron et al., 2014; Galaasen  
 412 et al., 2014; Pol et al., 2014). Also, the Belgian speleothems presented in this study reflect that conditions  
 413 for speleothem growth were better after 125 ka.

#### 414 5.4 Glacial inception and Eemian-Weichselian transition: a climatic event at 117.7 ka

##### 415 5.4.1 Chronological constraints

416 The Han-8 and Han-9 tuned age-depth models allow a detailed investigation of the timing and rate of  
 417 the Eemian-Weichselian Transition. The EWT in Han-9 was originally identified as the transition from  
 418 forest vegetation to a more grass and shrub like vegetation, causing a decrease in vegetation derived soil  
 419  $\text{CO}_2$  which is reflected in the carbon isotopic record. This transition was linked to the Late Eemian Aridity  
 420 Pulse, recognized in the Eifel pollen records located only 150 km from the cave site (Sirocko et al., 2005).  
 421 Based on the tuned age-depth model, the  $\delta^{13}\text{C}$  increase in Han-9 and Han-8 starts at  $117.7 \pm 0.5$  ka. In  
 422 RSM-17, a  $\delta^{13}\text{C}$  excursion with similar magnitude occurs at  $118.1 +0.4/-0.3$  ka. Despite a small offset in  
 423 timing (Fig. 3), although an overlap in the  $2\sigma$  error of both ages is present, the  $\delta^{13}\text{C}$  excursion in RSM-17  
 424 is considered to represent the same event as the  $\delta^{13}\text{C}$  excursion in the Han-sur-Lesse speleothem records.  
 425 Because of the higher precision of the Han-8 and Han-9 age-depth models, the age of  $117.7 \pm 0.5$  ka is  
 426 adapted for the onset of this event. Although the increase in  $\delta^{13}\text{C}$  is not entirely monotonic in both Han-  
 427 sur-Lesse records, a total increase of  $\sim 4\text{‰}$  is accommodated in about 0.2 ka, before the start of the  
 428 discontinuity in both records at  $117.5 \pm 0.5$  ka. Due to the occurrence of growth interruptions in the Han-  
 429 sur-Lesse speleothems, it is difficult to establish the duration of the event. Yet varve counting on the  
 430 nearby ELSA record (Eifel, Germany) has provided a duration of 468 varve years for the LEAP (Sirocko  
 431 et al., 2005).

#### 432 5.4.2 Paleoclimate changes during the glacial inception

433 The newly added records of Han-8 and RSM-17 allow to investigate the paleoclimate changes during  
 434 the glacial inception. Looking at Han-8  $\delta^{13}\text{C}$ , the increase in centennial, large-amplitude variability after  
 435 the onset of the event at  $117.7 \pm 0.5$  ka is striking (Fig. 5). This is in clear contrast with more stable  $\delta^{13}\text{C}$   
 436 values before 117.7 ka. In Han-8, these variations in  $\delta^{13}\text{C}$  briefly return to pre-117.7 ka values  $-6.8 \text{‰}$  at  
 437 115.1 ka and 111.9 ka. In the RSM-17, similar observations are made with a larger variability before  
 438  $118.1 +0.4/-0.3$  ka. The increase in  $\delta^{13}\text{C}$  variability is interpreted to reflect increased degradation of soil  
 439 activity, caused instability of the vegetation assembly above the cave, rapidly switching between a dense  
 440 tree cover and more open grass and shrub vegetation. Since the Eemian in northwestern Europe is defined  
 441 as a warmer climate interval associated with the spread of temperate mixed forests in areas with similar  
 442 vegetation today (Kukla et al., 2002) and because of the distinct difference in  $\delta^{13}\text{C}$  isotopic signature  
 443 before and after 117.7 ka in all three investigated speleothem samples, the end of the Eemian, and thus the  
 444 Eemian-Weichselian transition in these records is set at  $117.7 \pm 0.5$  ka. Although short-lasting episodes of  
 445 forest recovery occur after 117.5 ka, e.g. at 115.1 and 111.9 ka (Fig. 5), millennial scale stable conditions  
 446 similar to that observed during the Eemian optimum ( $\sim 125$ -118 ka) are not observed anymore.

447Consequently, the onset of the glacial inception in the Belgian speleothem record, following the EWT, is  
448set at  $117.7 \pm 0.5$  ka.

449 The high-resolution records of RSM-17 provide additional insights in the paleoclimate changes  
450occurring at the EWT. Figure 6 show the changes in  $\delta^{13}\text{C}$  and Figure 7 shows the changes in trace element  
451concentrations. Figure 6 and 7 are plotted on a distance axis because of the higher uncertainty in the  
452RSM-17 age-depth model. Yet, the Han-sur-Lesse chronology has shown that the start of the  $\delta^{13}\text{C}$   
453excursion, and thereby the EWT, can be set at  $117.7 \pm 0.5$  ka. In RSM-17, this  $\delta^{13}\text{C}$  increase starts at  
454561.5 mm dft. At 561.5 mm dft, the speleothem morphology is still similar to that observed during the  
455Eemian optimum, i.e. thick layers consisting of an alternation between white porous calcite and brown,  
456dense calcite (Fig. 2 and Fig. 6). This is in contrast with the internal speleothem morphology of RSM-17  
457that is observed after 545 mm dft, consisting of white porous calcite containing only very thin laminae  
458(Fig. 6). This severe reduction in layer thickness evidences a decrease in growth rate of RSM-17 at that  
459time. The increase in  $\delta^{13}\text{C}$ , from -12.5 to -8 ‰, starts at 561.5 mm dft. However, it is not until 545 mm dft  
460mm that the morphology of the speleothem suddenly changes (Fig. 6). Taking into account that the layers  
461are annual (see section 6.1), layer counting indicates that speleothem morphology changes at least 18  
462years after the start of the  $\delta^{13}\text{C}$  increase (Fig. 6), implying that vegetation started changing before a  
463decrease in speleothem growth rate took place. This has important consequences for the paleoclimatology  
464of the late event starting at  $117.7 \pm 0.5$  ka. The term ‘late Eemian aridity pulse’, which is the equivalent of  
465this event in the Eifel region (Germany), refers to a dry event, yet it was interpreted as ‘an event with dust  
466storms, aridity, bushfire and a decline in thermophilous trees by a decrease in both precipitation and  
467temperature’ (Sirocko et al., 2005). In case of RSM-17, the lead of the vegetation switch, shown by the  
468increase in  $\delta^{13}\text{C}$ , on the change speleothem in morphology and thus growth rate suggests that the event is  
469initiated by a drop in temperature rather than a drop in precipitation amount. If a decrease in precipitation  
470initiated the event, the  $\delta^{13}\text{C}$  and the growth rate would change at the same time. Following an initial cold  
471pulse, vegetation changes from a tree-dominated assembly towards a grass/shrub dominated assembly.  
472Due to this change in biomass, vegetation-derived  $\text{CO}_2$  in the soil, originating from root respiration and  
473degrading soil organic matter, lowers. This in turn lowers the dissolved  $\text{CO}_2$  in the waters infiltrating the  
474epikarst. The  $\text{CO}_2$  decrease renders the infiltrating waters less acidic and diminishes the potential of  
475limestone dissolution, eventually leading to a decreased  $\text{Ca}^{2+}$  content of the drip water resulting in a  
476decreased growth rate. This is also reflected in the Han-8 and Han-9 speleothems: the hiatus only starts at  
477 $117.5 \pm 0.5$ , which is 0.2 ka after the decrease in  $\delta^{13}\text{C}$ . Further evidence supporting the hypothesis that the  
478event is initiated by a cold pulse and that decreased precipitation lags this cold pulse is provided by trace  
479element variations in RSM-17 (Fig. 7). Right at the point where the RSM-17 morphology changes from

480thick annual layers to very fine laminae, identified to reflect the change in water availability (red line in  
 481Fig. 7), Mg increases while Sr and Ba decrease. Variations of host rock derived trace elements in  
 482speleothems, such as Mg, Sr and Ba, have often been interpreted to reflect changes in prior calcite  
 483precipitation (e.g. Fairchild and Treble, 2009). Prior calcite precipitation (PCP) is the process of calcite  
 484precipitation upstream of the site of speleothem deposition, and predominantly occurs during dryer  
 485periods (Fairchild et al., 2000; Fairchild and Treble, 2009). In RSM-17, Mg concentrations increase from  
 486~150  $\mu\text{g g}^{-1}$  to 300  $\mu\text{g g}^{-1}$  at approximately 545 mm dft (Fig. 7). This increase does not occur simultaneous  
 487with the increase in  $\delta^{13}\text{C}$  at 561.5 mm dft (Fig. 6), but it starts where the change in speleothem  
 488morphology is observed (Fig. 6), suggesting a similar control on Mg variations and growth rate. The  
 489observed changes in Mg concentration fit with the process PCP, with higher concentrations during periods  
 490with less water availability and thus lower growth rates. Concentrations of Sr and Ba behave opposite  
 491with respect to Mg, suggesting no control of PCP on Sr and Ba. Dolomite dissolution has been evoked in  
 492the past to explain an antiphase behavior of Mg and Sr (Roberts et al., 1998), even in Han-sur-Lesse cave  
 493(Vansteenberghe et al., in review). However, Mg concentrations in RSM-17 average at 194  $\mu\text{g g}^{-1}$ , which is  
 494very low and questions the influence of dolomite in the host rock on the speleothem geochemistry. A more  
 495likely mechanism controlling Sr and Ba variations in RSM-17 is the speleothem growth rate.  
 496Experimental studies have shown that the partitioning of Sr in calcite increases with the precipitation rate  
 497(Lorens, 1981; Pingitore and Eastman 1986). Yet, from cave-analogue experiments Day and Henderson  
 498(2013) concluded that growth rate changes smaller than a factor 2.5 are unlikely to have any effect on the  
 499partitioning of Sr in cave calcite. However, if RSM-17 layer thickness is presumed to act as a proxy for  
 500growth rate, a decrease in growth rate by a factor  $>2.5$  at the morphological transition is definitely  
 501plausible (Fig. 6-7). In a similar way, Bourdin et al. (2011) interpreted changes in earth-alkaline elements,  
 502and more specific an antiphase behavior of Mg versus Sr and Ba, in a stalagmite from Chauvet Cave  
 503(France) as a result of changes in growth rate. It is concluded that in the case of RSM-17, Mg variations  
 504reflect a changing amount of PCP in the epikarst while the effect of growth rate dominates over PCP for  
 505controlling variations in Sr and Ba concentrations. The U concentration in RSM-17 is also lower after 545  
 506mm dft (Fig. 7). Bourdin et al. (2011) suggested that the main source of U in speleothem drip waters is  
 507limestone dissolution. The observed lower U concentrations in RSM-17 are thus in agreement with  
 508decreased bedrock dissolution at a time when lower growth rates are observed after 545 mm dft.

509 At 545 mm dft, the amplitude of variation in P and Y diminishes severely (Fig. 7). In speleothems, P  
 510originates from vegetation dieback (Fairchild et al., 2001; Huang et al., 2001, Treble et al., 2003; Borsato  
 511et al., 2007) and is transported towards the speleothem via the binding to organic acids. Although  
 512vegetation is believed to constitute the main source of P concentration in speleothems, leaching of



phosphate minerals in the epikarst has also been identified as a process that potentially contributes P to speleothems (Frisia et al., 2012). Yttrium is commonly transported into speleothems by binding to natural organic matter (Borsato et al., 2007; Hartland et al., 2012). The decrease in concentration of both elements in RSM-17 is therefore interpreted to reflect decreased amounts of organic matter within the soil, due to a lower vegetation productivity which is in agreement with the decreased vegetation activity interpreted from the  $\delta^{13}\text{C}$  record. Both P and Y concentrations are lower when the speleothem growth rate decreases. This confirms the influence of vegetation productivity and vegetation-derived soil  $\text{CO}_2$  on the speleothem growth rate. The Al and Zn display an increase at 550 mm dft, shortly after the morphological change. The paleoclimatological significance of Al is not commonly studied in speleothems, but Al variations likely reflect an enhanced detrital input into the speleothem, since Al is a major element in clay and fine detrital material and it is dominantly transported into speleothems via larger detrital particles (Fairchild and Treble, 2009). Increased detrital input can result from increased accumulation of fine particles in dryer cave environments, rather than through the drip water. Zinc behaves opposite to Y, with higher concentrations after 50 mm. Yet, previous studies have shown that Zn, like Y, is preferentially transported into speleothems through binding to natural organic matter (Hartland et al., 2012; Wynn et al., 2014). Because Zn concentration shows similar trends as Al concentration within the speleothem, Zn is interpreted to have detrital signature, similar to Al, rather than an organic matter signature, such as Y.

#### 5.4.3 Regional to global significance of the 117.7 ka event

Numerous paleoclimate records have reported the presence of a short-lasting and drastic climate event at the end of the Eemian or MIS 5e. The 117.7 ka event as observed in the Belgian speleothems can be related to most of these late Eemian/MIS 5e climate deterioration or events observed in other records (Fig. 8). Besides the earlier mentioned pollen record from the Eifel at  $118 \pm 1$  ka (Sirocko et al., 2005, Fig. 8), a brief reduction in forest cover occurring between 118.2 and 117.5 ka was also identified in Ioannina and Kopais pollen records, Greece (Tzedakis et al., 2003). In lake cores retrieved from Lago Grande di Monticchio (Italy) a slight decrease in the percentage of woody taxa pollen is observed at between 118 and 117 ka (Fig. 8, Brauer et al., 2007; Allen and Huntley, 2009). Additional temperature reconstructions based on pollen records from La Grande Pile (France) and Lago Grande di Monticchio (Italy) have indicated that at ~117-118 ka a short temperature decrease occurs that fits with the event observed in the Belgian speleothems. Precipitation reconstructions show a simultaneous decrease in precipitation, yet in contrast to temperature, precipitation does not recover after the event (Brewer et al., 2008). In the La Grande Pile pollen record (Vosges, France) a cold and dry event, the Woillard event (Kukla et al., 1997), was identified just before the end of the Eemian, characterized by a rapid replacement of the temperate hardwood forest by boreal vegetation (Woillard, 1978). Similar vegetation

546 changes in pollen records from eastern Poland (Granoszewski, 2003) were likewise correlated to the  
 547 Woillard event by Helmens (2014). However, because Eemian vegetation is suspected to last longer in  
 548 southern Europe (Müller and Sanchez Goñi, 2007), the Woillard event is generally placed later in those  
 549 records (e.g. Brauer et al., 2007). Despite the clear presence of the 117.7 ka event in European pollen  
 550 records, the event is still underrepresented in European speleothem records. To the extent of our  
 551 knowledge, the event can be correlated with only two other speleothem records. The first is the TKS  
 552 flowstone retrieved from the Entrische Kirche in the Austrian Alps (Fig. 1a, Meyer et al., 2008). The TKS  
 553  $\delta^{18}\text{O}$  displays a fast,  $\sim 4\text{‰}$  decrease in  $\delta^{18}\text{O}$  centered at  $118 \pm 2$  ka (Fig. 8), which was interpreted to  
 554 reflect a strong cooling. However, in the TKS  $\delta^{13}\text{C}$  no excursion similar to that observed in the Belgian  
 555 speleothem datasets is present. The second dataset contains the BAR-II duplicate speleothem record  
 556 (Demény et al., 2017). The BAR-II speleothem was retrieved from the Baradla Cave, northeastern  
 557 Hungary. The BAR-II  $\delta^{18}\text{O}$  shows a sudden decrease at  $117.0 \pm 0.8$  ka (Fig. 8), interpreted to reflect an  
 558 arid pulse. At the same time, a  $\sim 2\text{‰}$  increase is observed in the  $\delta^{13}\text{C}$ . Other European speleothem  
 559 records, such as the Corchia Cave speleothems (Drysdale et al., 2005; 2007), speleothems from the Alps  
 560 (Boch et al., 2011; Moseley et al., 2015) and speleothems from the Levant (Bar-Matthews et al., 2003;  
 561 Nehme et al., 2015), do not record any anomalies in their stable isotope proxies.

562        Besides (European) continental records, clear evidence from high-resolution marine sediment  
 563 archives of a climate anomalous event around 117 to 118 ka in the North Atlantic realm exists. The  
 564 presence of a cold event at the Eirik Drift, South of Greenland in the North Atlantic Ocean (Fig. 1a),  
 565 which occurs just before the end of the MIS 5e benthic  $\delta^{18}\text{O}$  plateau, is reported by Galaasen et al. (2014)  
 566 and Irvali et al. (2016). More specific, an increase in  $\delta^{18}\text{O}$  of planktonic foraminifera and an increase in  
 567 the amount of ice rafted debris (IRD) occur at  $\sim 117$  ka in marine sediment core MD03-2664, indicating  
 568 the presence of colder conditions in that area (Fig. 9). According to the age model presented in Irvali et al.  
 569 (2016), this event lasts about 0.4 ka, which is similar to the LEAP observed in the ELSA record (Sirocko  
 570 et al., 2005). High-resolution  $\delta^{13}\text{C}$  analysis of epibenthic foraminifera (*C. wuellerstorfi*, Fig. 9) indicates  
 571 that during this event, the formation of North Atlantic Deep Water was reduced, which is believed to be  
 572 the cause of the cold conditions during the event (Galaasen et al., 2014). In the Bermuda Rise (western  
 573 Atlantic Ocean, Fig. 1a), similar observations were made, i.e. an increase in Cd/Ca and clay flux indicates  
 574 a shift in deep oceanographic conditions with an increased input of southern source waters compared to  
 575 NADW (Fig. 9). This shift occurred in approximately 400 years at  $\sim 118$  ka (core MD95-2036; Adkins et  
 576 al., 1997). Later on, Lehman et al. (2002) calculated  $\sim 3\text{°C}$  decrease in sea surface temperature in MD95-  
 577 2036 at  $\sim 118$  ka. A core retrieved from the Norwegian Sea (ODP-980; Oppo et al., 2006) shows a distinct  
 578 decrease in sea surface temperature and lithic fragments at  $\sim 118$  ka. It is thus apparent that an event,

579equivalent to that observed in the Belgian speleothems at  $117.7 \pm 0.5$  ka, is occurring in the North Atlantic  
580region. In particular, the increase in IRD in sediment cores reflects growth regional ice sheet growth  
581(Irvali et al., 2016). Global sea-level reconstructions inferred from coastal deposits (e.g. corals) indicate a  
582rapid fall of the above-present sea-level at the end of MIS 5e after 118 ka (Fig. 9, Hearty et al., 2007),  
583indicating the rapid growth of ice sheets at that time. More precise ages are provided by Moseley et al.  
584(2013), who inferred from presently submerged speleothems of the Yucatan peninsula that MIS 5e sea-  
585level dropped to -4.9 m by  $117.7 \pm 1.4$  ka.

586        However, the age-depth models of these marine records are often constructed using climato-  
587stratigraphic alignment strategies (Govin et al., 2015) and the chronology of these records is therefore not  
588absolutely and independently constrained. Yet, the similarity in timing, duration and climatologic  
589expression suggests that Belgian speleothems, European pollen archives and marine sediment cores from  
590the North Atlantic realm registered the same climatic event. So what could have caused such a widespread  
591rapid, short-lasting cooling event as observed in the Belgian speleothems at  $117.7 \pm 0.5$  ka and other  
592continental European and North Atlantic records? The presence of Eemian optimum conditions between  
593125-120 ka is evident from several European paleoclimate reconstructions (Fig. 8 and section 6.3). Such  
594optimum conditions at that time caused a significant degree of ice mass loss, resulting in peak eustatic  
595sea-levels up to +6 to +9 m between ~120 and 118 ka compared to present (Fig. 9). This peak in eustatic  
596sea-level, 2 to 6 m above the MIS 5e average sea-level (Hearty et al., 2007; Blanchon et al., 2009; Dutton  
597and Lambeck, 2012; O'Leary et al., 2013; Sivan et al., 2016), would require melting of a substantial  
598amount of the Greenland ice sheet and perhaps even a small contribution by melting of the West Antarctic  
599ice sheet (Hearty et al., 2007). This enhanced melting would induce a significant input of freshwater in  
600the North Atlantic. In model simulations, a large freshwater flux resulting from the northern hemisphere  
601ice sheet loss leads to a temporary abrupt weakening of the Atlantic meridional overturning circulation  
602(AMOC), causing a strong decrease in global annual mean temperature (Loutre et al., 2014). Potential  
603evidence for a reduced formation of NADW related to AMOC weakening during the 117.7 ka event, has  
604been found in the sediment core from the Erik Drift, South of Greenland (Galaasen et al., 2014). In the  
605frame of these findings, the cooling event at  $117.7 \pm 0.5$  ka that resulted in a vegetation shift observed in  
606the Belgian speleothems, is due to weakening of the AMOC and reduction of NADW formation. This  
607cooling event crossed a critical threshold for a vegetation shift towards a decrease in tree species to occur  
608in Western Europe at 117.7 ka, which is evident from the speleothems'  $\delta^{13}\text{C}$  record.

#### 6096.5 Early Weichselian millennial climate variability (117.5 – 100 ka)

During the glacial inception, which is set at 117.7 ka, with the start of the cold event detected in the Belgian speleothem records, an increased variability in  $\delta^{13}\text{C}$ , suggesting increased vegetation instability, is observed. In Han-8, other proxies such as  $\delta^{18}\text{O}$  and Mg, Sr, Ba and also U show a more gradual decrease towards minimum values at  $\sim 114.3$  ka (Fig. 5). These proxies reflect a gradual decline of interglacial paleoclimate conditions characterizing the glacial inception. The timing of appearance of this gradual decline is in line with observations from other records in continental Europe and the North Atlantic (Fig. 8 and 9). Han-8  $\delta^{18}\text{O}$  and Mg, Sr, Ba and U remain at a minimum until  $\sim 112$  ka. At the same time of this minimum observed in the speleothem records, a slightly warmer stadial period occurs in Greenland, i.e. Greenland Interstadial (GI) 25. In this study, the NGRIP  $\text{d18O}$  data is plotted on the GICC05modelext timescale (Wolff et al., 2010). This chronology is preferred over the AICC2012 (Bazin et al., 2013; Veres et al., 2013) because of 1) the proximity of the Greenland ice core archives over the Antarctic ice core archives (Govin et al., 2015) and 2) the synchronous appearance between Greenland Stadials 25 and 24 in NGRIP record on a GICC05modelext timescale and the expression of these stadials in continental Europe recorded in Alpine speleothems (Boch et al., 2011). Capron et al. (2010) showed that the GI-25 warming in Greenland is of significantly lower amplitude than the following interstadial events ( $3 \pm 2.5$  °C compared to 8-16 °C) and concluded that GI-25 represents a local climate feature in Greenland rather than later global interstadial events. This implies that GI-25 did not persist in continental Europe, and confirms why there is no distinct signature of a GI-25 equivalent event in the speleothem record. Other European speleothems and pollen records (Fig. 8), do not show a distinct GI-25 equivalent signature as well, evidencing that this stadial was not as prominent as the following GI-24. Yet, at  $\sim 112$  ka, Han-8  $\delta^{18}\text{O}$  and Mg, Sr, Ba and U increase again. This increase shows affinity with a short warming event observed at the end of GI-25, defined as 'GIS 25s' (Capron et al., 2012), but later labeled as GI-25a by Ramsussen et al. (2014). It is remarkable, especially for the Han-sur-Lesse speleothems, that the stadial/interstadial events are reflected not only in the paleoclimate proxies (e.g. GS-25 in Han-9  $\delta^{13}\text{C}$ ) but also in the growth rate of the speleothems. For example, Han-8 stops growing at the start of GS-25 in the NGRIP record, and at the same time a severe decrease in growth rate is observed in Han-9 (Fig. 3). Moreover, the second hiatus in Han-9 corresponds in timing to GS-24. From the Han-9 growth rate (Fig. 3), it appears that the Han-9 speleothem never fully recovered from GS-25, and additional cooler-drier conditions at the onset of GS-25 were sufficient to cease speleothem formation (Vansteenberghe et al., 2016).

## 6406. Conclusions

641 Following conclusions are reached:

1. The two newly added Belgian speleothem records Han-8 and RSM-17 confirm the general climatic trends of the Eemian to early Weichselian observed in Han-9. Especially the reproducibility of the Han-9  $\delta^{13}\text{C}$  record with the coeval Han-8 speleothem is remarkable, confirming the hypothesis of Vansteenberghe et al. (2016) that  $\delta^{13}\text{C}$  represents a regional climate signal controlled by vegetation activity, reflecting vegetation assembly above the cave.
2. These two newly studied speleothems also show rapid increase in  $\delta^{13}\text{C}$ , similar to the earlier observed rapid 4 ‰ increase in Han-9  $\delta^{13}\text{C}$  at  $117.5 \pm 0.5$  ka. This  $\delta^{13}\text{C}$  increase in Han-9 was interpreted to represent a rapid change in vegetation, from dominated by temperate tree species towards dominated by grasses and shrubs which was caused by fast cooling and/or drying of the regional climate. This event shows a strong affinity in terms of timing and climatic expression with the Late Eemian Aridity Pulse (LEAP), identified in the nearby ELSA vegetation stack and characterized by an increase in grass pollen and loess content at  $118 \pm 1$  ka (Sirocko et al., 2005). Aligning the chronologies of the two independently dated Han-sur-Lesse speleothem records (Han-8 and Han-9) assign a more precise absolute age of  $117.7 \pm 0.5$  ka to the start of this event. In both speleothems, a hiatus starts at  $117.5 \pm 0.5$  ka hampering the assessment of the duration, yet in the ELSA stack the LEAP lasts 468 varve years.
3. The start of the 117.7 ka event in the Belgian speleothems marks an important boundary in the Belgian speleothem proxies between Eemian optimum conditions and increased variability during the glacial inception. The start of this event at  $117.7 \pm 0.5$  ka is therefore proposed as the Eemian-Weichselian transition (EWT) and consequently the start of the glacial inception as registered in the Belgian speleothems and potentially other records in northwestern Europe. This shows the importance of the event, at least in the study area, as a contributor to the last interglacial to glacial transition.
4. High-resolution analysis of the annually layered Belgian speleothem RSM-17 shows that the  $\delta^{13}\text{C}$  excursion (and thus vegetation changes) at the EWT starts before a decrease in precipitation which is reflected by trace element concentrations and speleothem morphology. It is therefore hypothesized that the climatic event starting at  $117.7 \pm 0.5$  ka is initiated by a cooling pulse that altered vegetation assembly above the cave. A few decades after this cooling pulse, additional drying of the climate occurs.
5. An event similar to that observed in the Belgian speleothems at  $117.7 \pm 0.5$  ka event is also present as a short-lived cooling event in several North-Atlantic sediment archives. This indicates a larger regional persistence than previously thought. Through comparison with these sediment archives and global sea-level reconstructions, it is hypothesized that the origin of the cooling event at 117.7 ka is an internal climate response caused by the substantial amount of freshwater

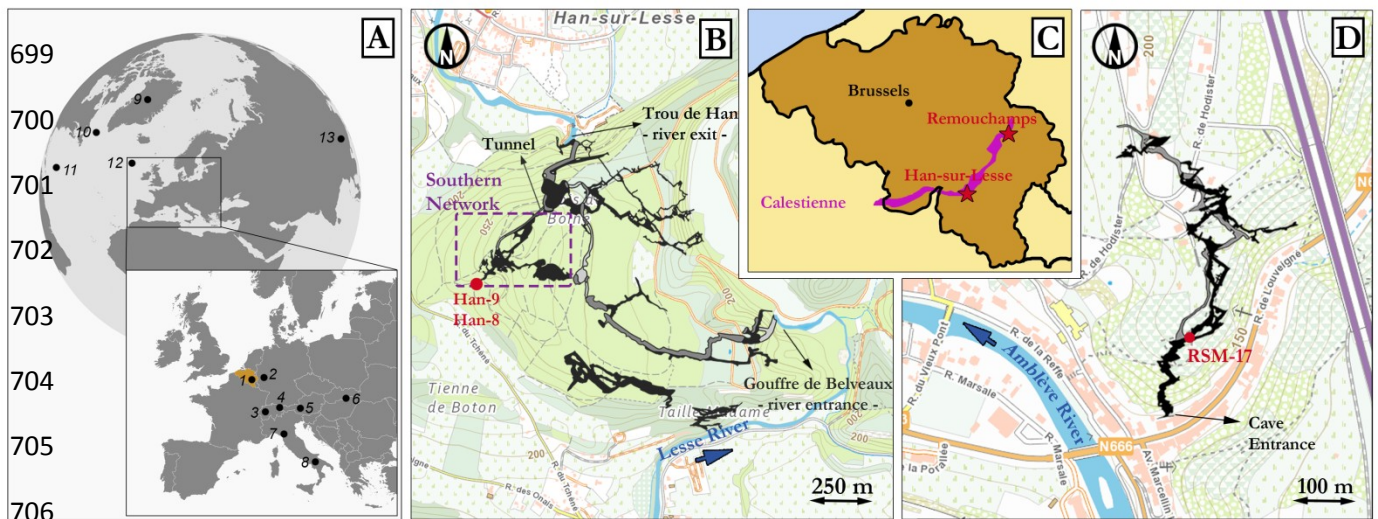
input from degraded ice-sheets by the end of the Eemian (~120-118 ka). This is also reflected by peak eustatic sea-level at the end of the Eemian.

6. The registration of this event by Belgian speleothems shows a clear climatic connection of these speleothems with other continental European archives and North Atlantic marine archives. This provides future potential of improving less constrained chronologies by alignment to the independently constructed speleothem age-depth models presented in this study.
7. Stadial-Interstadial changes are recorded by the speleothem paleoclimate proxies but are also tracked in the growth evolution of the speleothems. This shows that Belgian speleothems are very sensitive recorders of early glacial climate changes.

## Acknowledgements

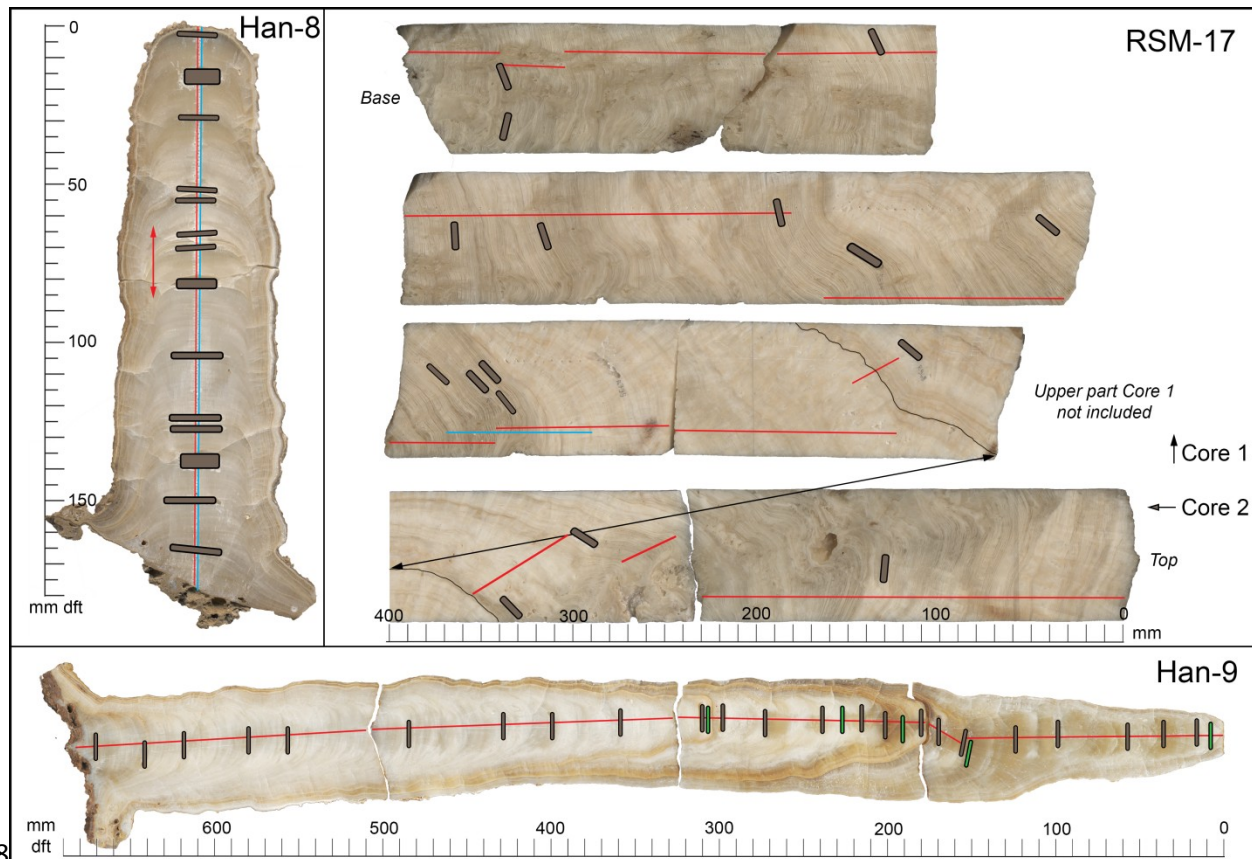
We thank M. Gewalt for the first analysis of RSM-17, as well as the cave management of Han-sur-Lesse and Remouchamps Cave for allowing us to retrieve the samples and study the cave environment. We also thank T. Goovaerts for the treatment of the speleothem samples, D. Verstraeten for the lab assistance at the VUB stable isotope lab and J.R.M. Allen and B. Huntley for providing the data of Lago Grande di Monticchio. S. Va. is funded by the VUB Strategic Research Program. P. C. thanks Hercules foundation for the upgrade of the VUB stable isotope lab. Han-8 speleothem was sampled in the frame of the EU H2020 Past4Future Project.

697**Figure 1**



707**Figure 1: (A) Location of the most important sites mentioned in the text (1) Han-sur-Lesse and**  
708**Remouchamps Cave (this study), (2) Eifel (Sirocko et al., 2005), (3 & 4) NALPS (Boch et al., 2011),**  
709**(5) Entrische Kirche (Meyer et al., 2008), (6) Baradla Cave (Demény et al., 2017), (7) Corchia Cave**  
710**(Drysedale et al., 2005; 2007; 2009), (8) Lago Grande di Monticchio (Brauer et al., 2007; Allen and**  
711**Huntley 2009), (9) NGRIP (NGRIP members, 2004), (10) MD03-2664 (Irvali et al., 2012; 2016;**  
712**Galaasen et al., 2014), (11) MD95-2036 (Adkins et al., 1997), (12) ODP-980 (Oppo et al., 2006) and**  
713**(13) Dongge Cave (Yuan et al., 2004). (B) Map of Han-sur-Lesse Cave based on Quinif (2006) (C)**  
714**Location of the Calestienne and the two cave sites in Belgium. (D) Map of Remouchamps Cave**  
715**based on (Ek, 1970).**

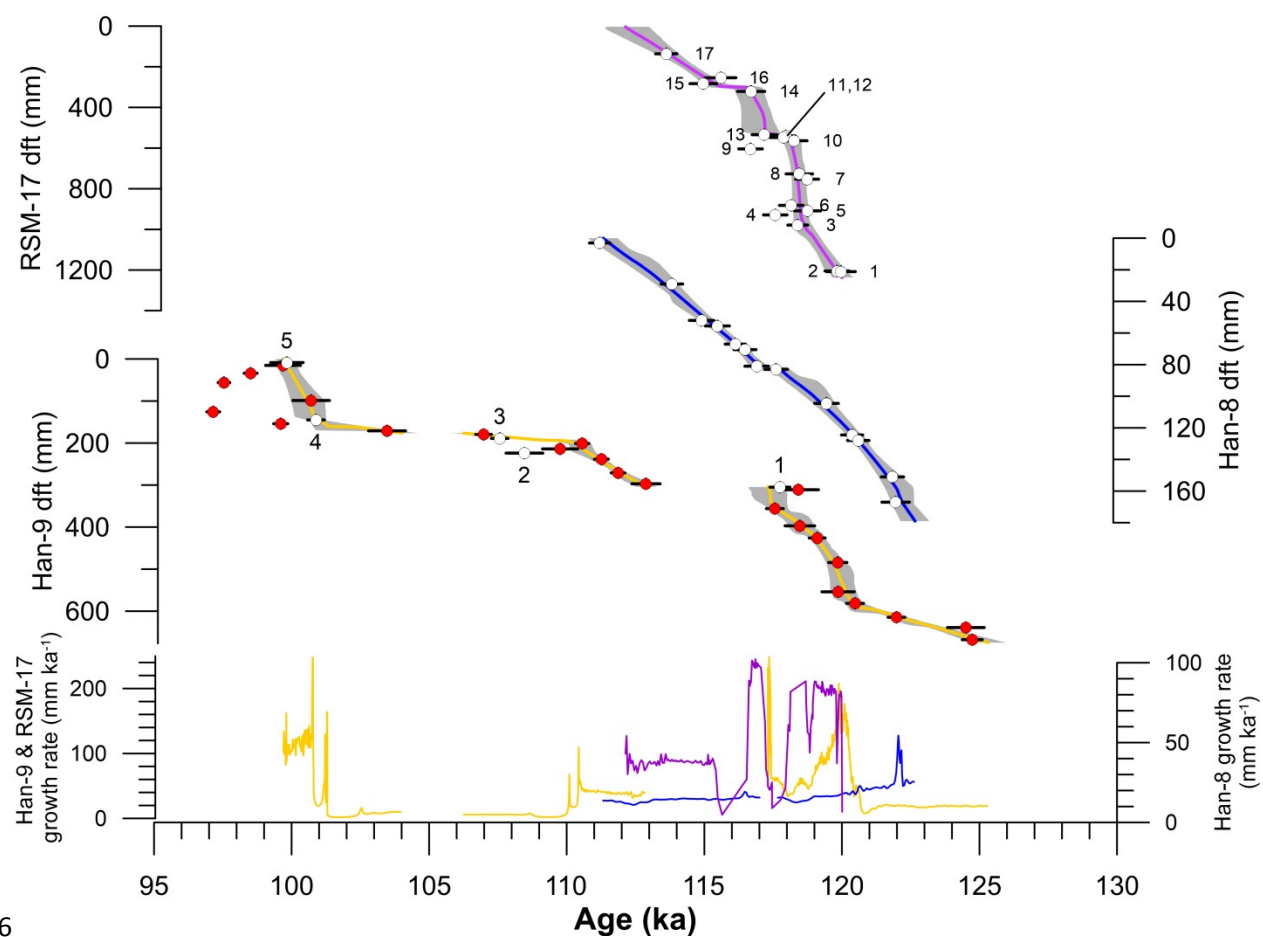
717**Figure 2**



719**Figure 2: Images of the samples used in this study. Red lines mark the location of the stable isotope**  
720**measurements and blue lines indicate the trace element transects. Grey boxes show the location of**  
721**the U-Th dating samples. Green boxes on Han-9 indicate the additional dates added in this study to**  
722**improve the original age-depth model of Vansteenberg et al. (2016). Black line in RSM-17 indicates**  
723**the marker layer that was used to correlate Core 1 and 2.**



725 **Figure 3**

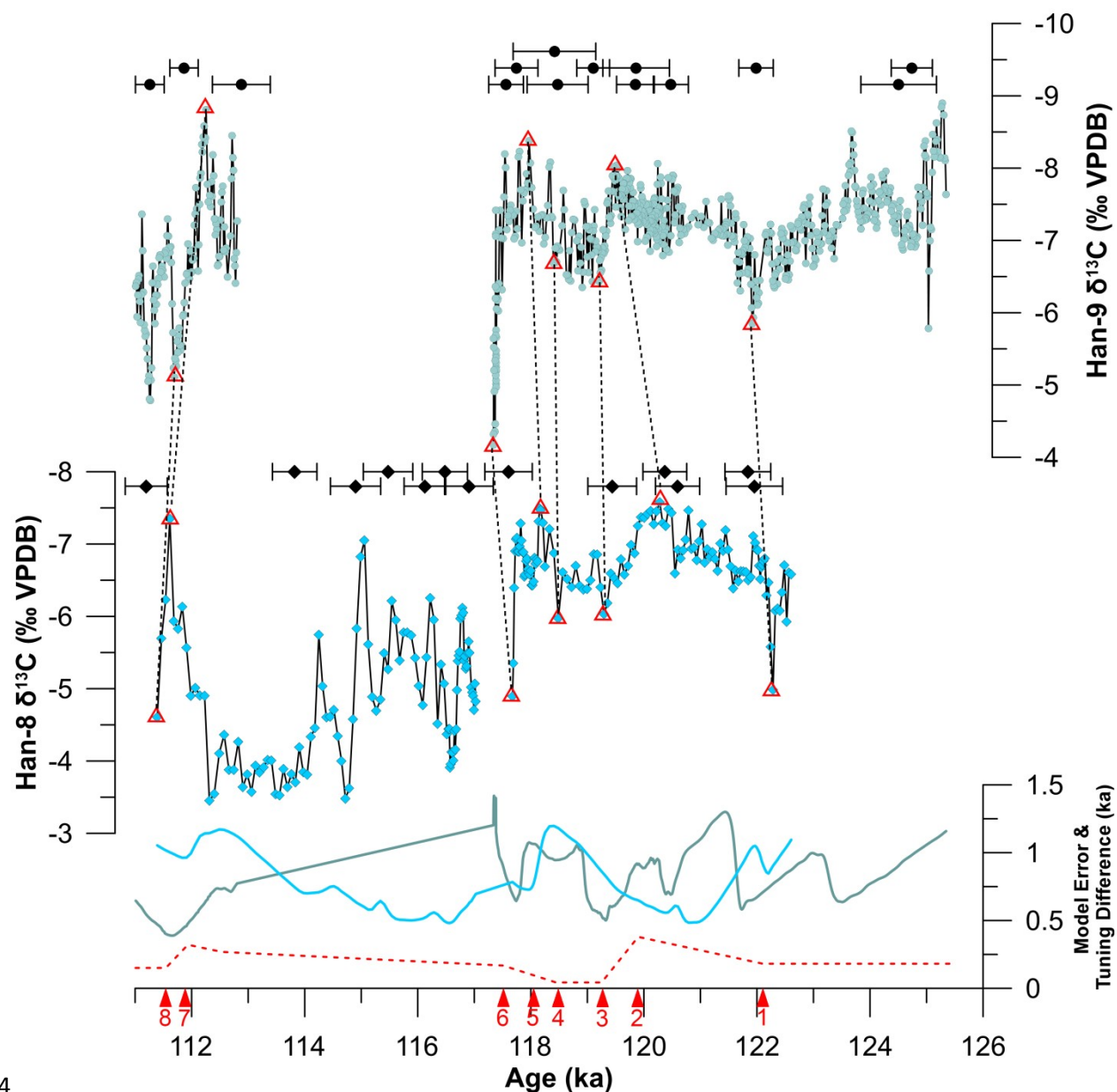


726

727 **Figure 3: U-Th dating results and calculated age-depth models of RSM-17 (purple), Han-8 (blue)**  
 728 **and Han-9 (yellow). Grey bands denote the  $2\sigma$  error. Red U-Th labels mark previously published**  
 729 **ages by Vansteenberg et al. (2016). Lower graph represents the growth rate of the speleothems in**  
 730  **$\text{mm ka}^{-1}$ . The ages discussed in the text are indicated by numbers.**

731

732



734

735Figure 4: Tuning of Han-9 and Han-8 age-depth models based on their  $\delta^{13}\text{C}$  record. Dark blue curve  
 736is the Han-9  $\delta^{13}\text{C}$  and light blue is Han-8  $\delta^{13}\text{C}$ . U-Th data is shown with black circles (Han-9) and  
 737diamonds (Han-8). Red triangles indicate the 8 tuning points, and the specifics are provided in  
 738Table 2. Lower graph shows the  $2\sigma$  error of the individual age-depth models (dark and light blue)  
 739and the dashed red line represents the age difference between the original Han-9 age-depth model  
 740and the tuned Han-9 age-depth model. See Table 2 for more information about the assigned tie-  
 741points.

742

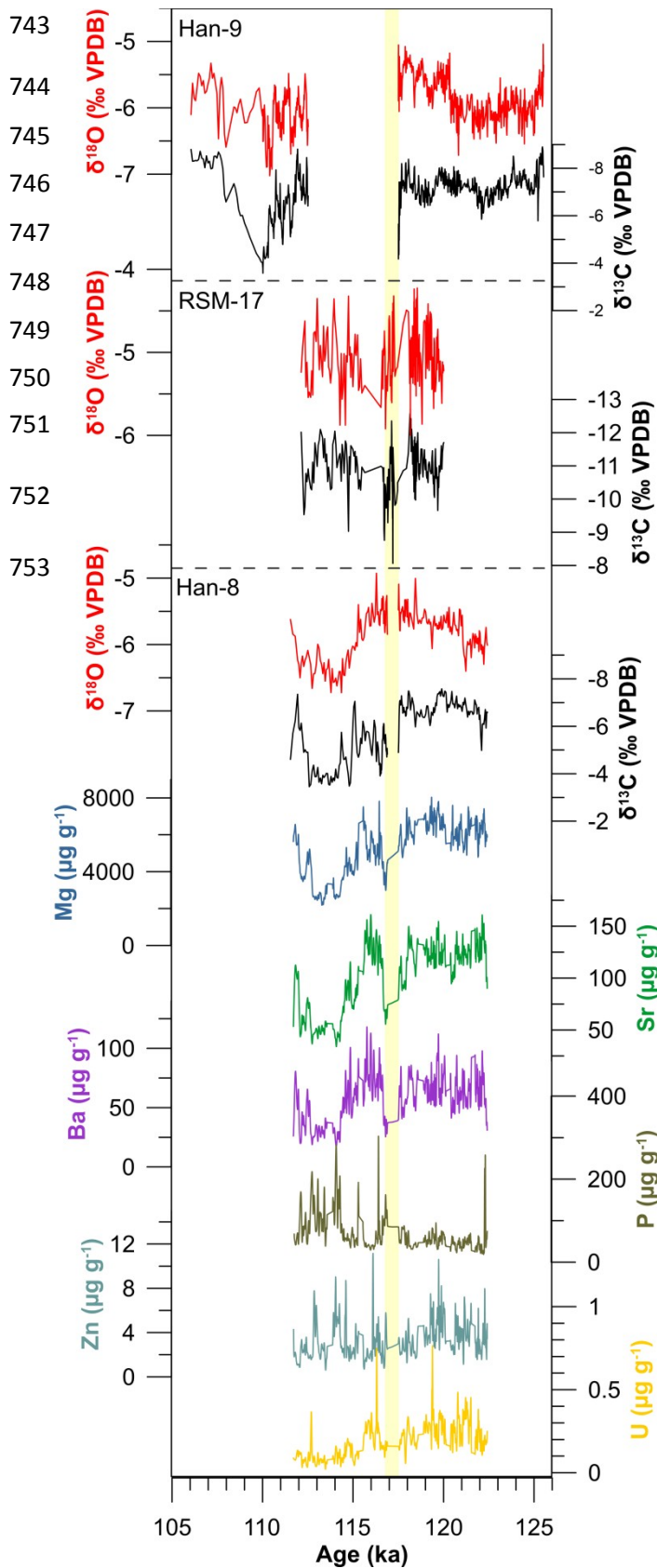
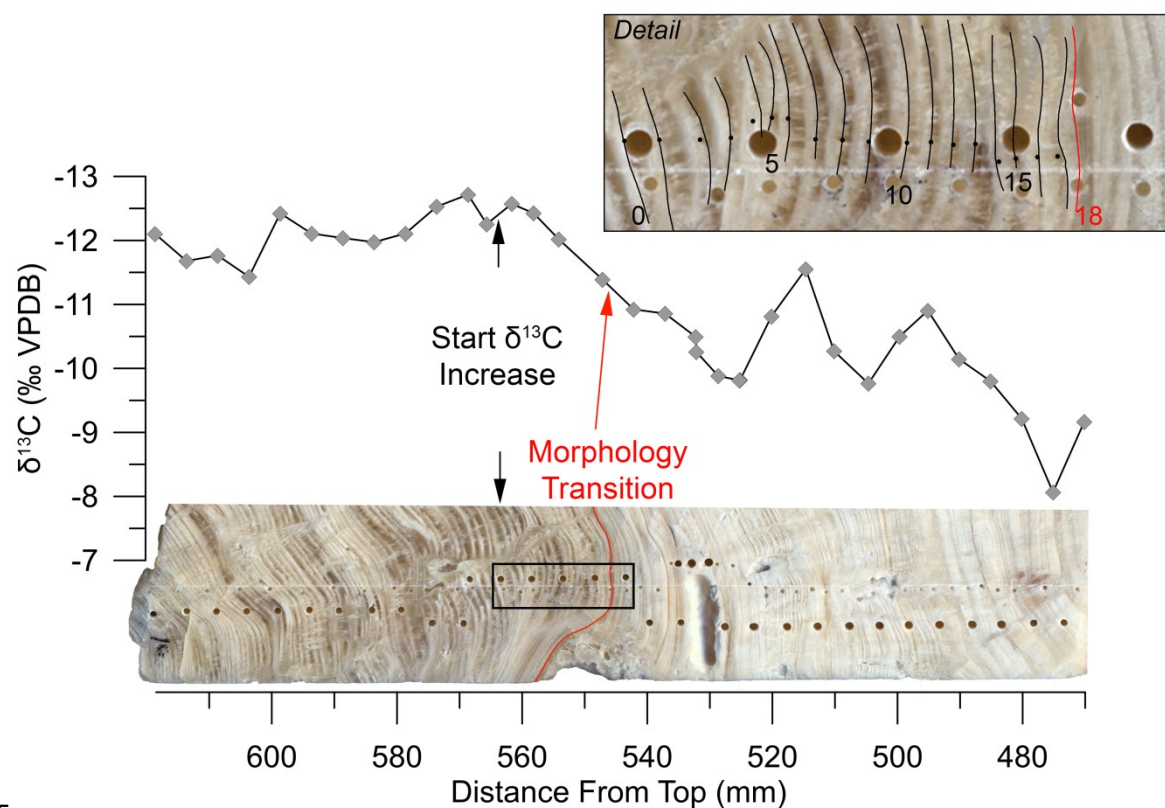


**Figure 5: Time-series of the speleothem proxies. Upper: Han-9  $\delta^{13}\text{C}$  (black) and  $\delta^{18}\text{O}$  (red) plotted on the tuned age-model. Middle: RSM-17  $\delta^{13}\text{C}$  (black) and  $\delta^{18}\text{O}$  (red). Lower: Han-8  $\delta^{13}\text{C}$  (black),  $\delta^{18}\text{O}$  (red), Mg (blue), Sr (green), Ba (purple), P (brown), Zn (light blue) and U (yellow) plotted on the tuned age-model. Yellow shading indicates the event at 117.7 ka.**

754 **Figure 6**

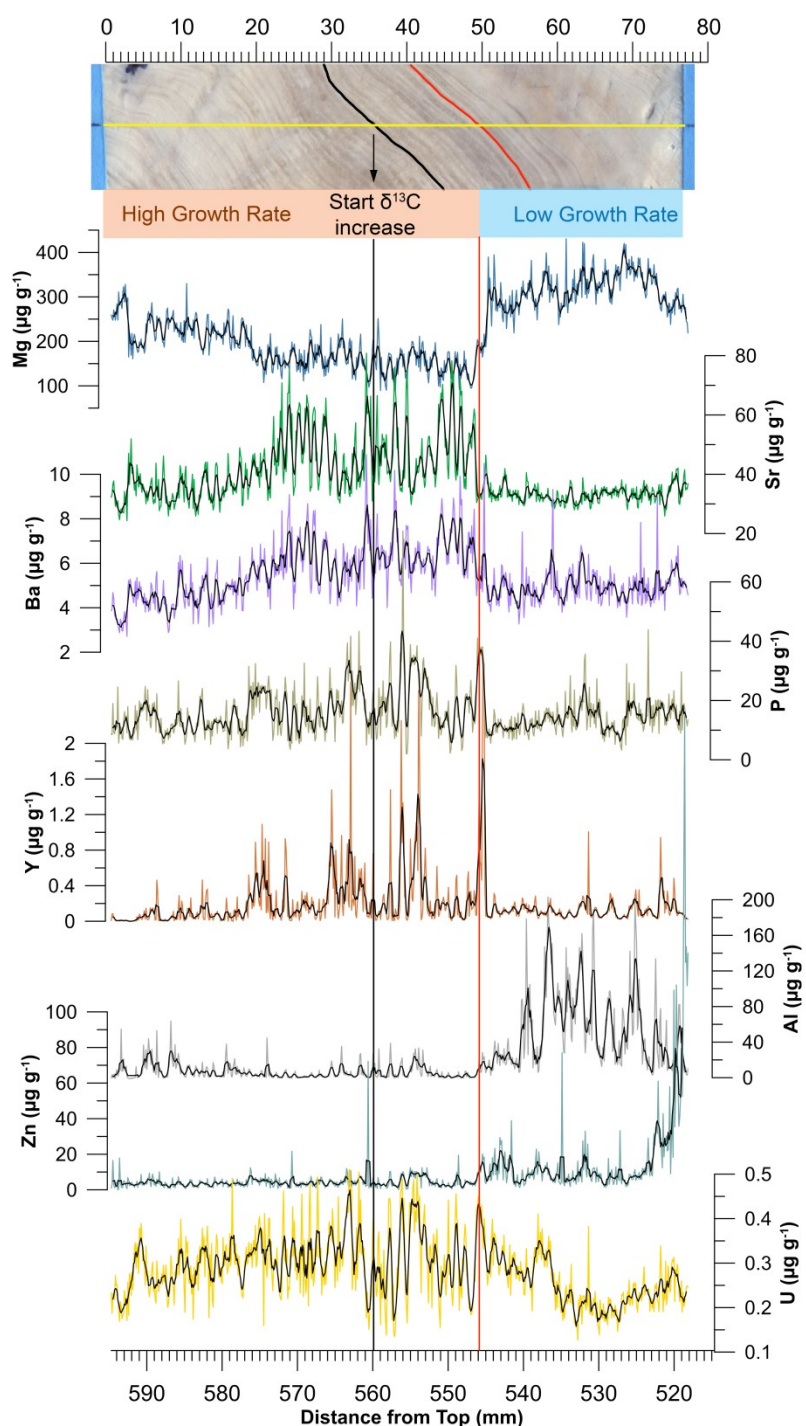


755

756 **Figure 6:**  $\delta^{13}\text{C}$  (grey) of RSM-17 over the Eemian-Weichselian transition plotted versus distance  
 757 from top in mm. Left is the oldest part of the speleothem and right the youngest. The increase of  
 758  $\delta^{13}\text{C}$  is observed before the morphology of the speleothem starts changing (red line). The insert  
 759 shows a detail of the annual layering, with the layer counting included.

760

761



762

763Figure 7: LA-ICP-MS trace element concentrations in  $\mu\text{g g}^{-1}$  of RSM-17 over the Eemian-  
 764Weichselian transition plotted versus distance from top in mm. The image shows a detailed scan of  
 765the annual layering around the EWT. Yellow line indicates the location of the trace element  
 766measurements. Black line indicates where the  $\delta^{13}\text{C}$  starts to increase (Fig. 7) and red line indicates

767where the speleothem morphology changes. The change in speleothem morphology, from thick  
768layers on the left to very fine laminae on the right, is interpreted to reflect a changing speleothem  
769growth rate. Blue: Mg, green: Sr, purple: Ba, brown: P, orange: Y, grey: Al, light blue: Zn and  
770yellow: U.



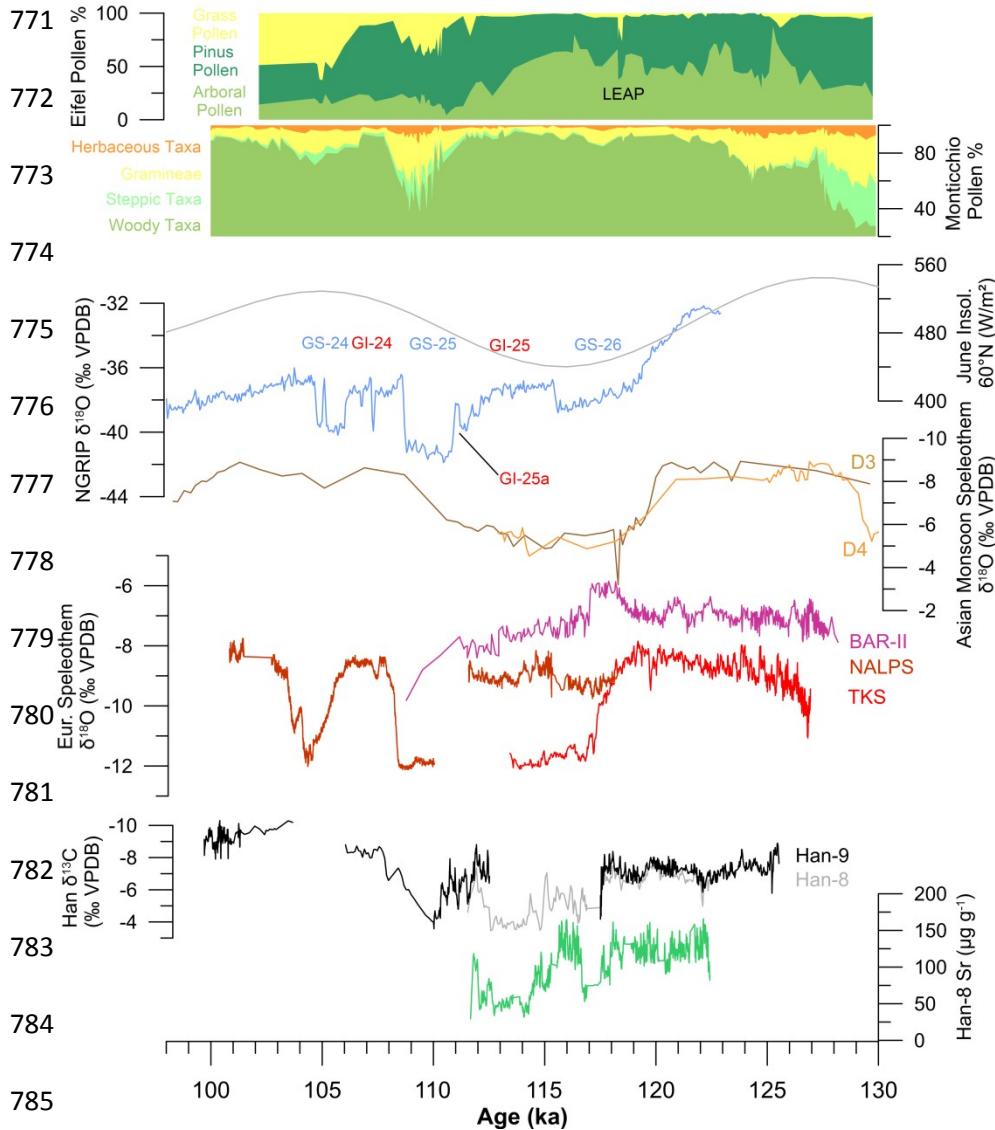


**Figure 8: Continental records covering the studied time frame. (A) Eifel grass, pinus and arboreal pollen abundance with the LEAP indicated (Sirocko et al., 2005). (B) Pollen abundances of herbaceous, grass, steppic and woody taxa from Lago Grande di Monticchio (Brauer et al., 2007; Allen and Huntley, 2009). (C) June insolation at 60° N. (D) NGRIP  $\delta^{18}\text{O}$  (NGRIP members, 2004) plotted on the GICC05modelext timescale (Wolff et al., 2010). (E) Asian monsoon intensity represented by Chinese speleothem  $\delta^{18}\text{O}$  (Yuan et al., 2004). (F) European speleothem  $\delta^{18}\text{O}$ . (G) Han-9  $\delta^{13}\text{C}$ , Han-8  $\delta^{13}\text{C}$  and Han-8 Sr concentration.**

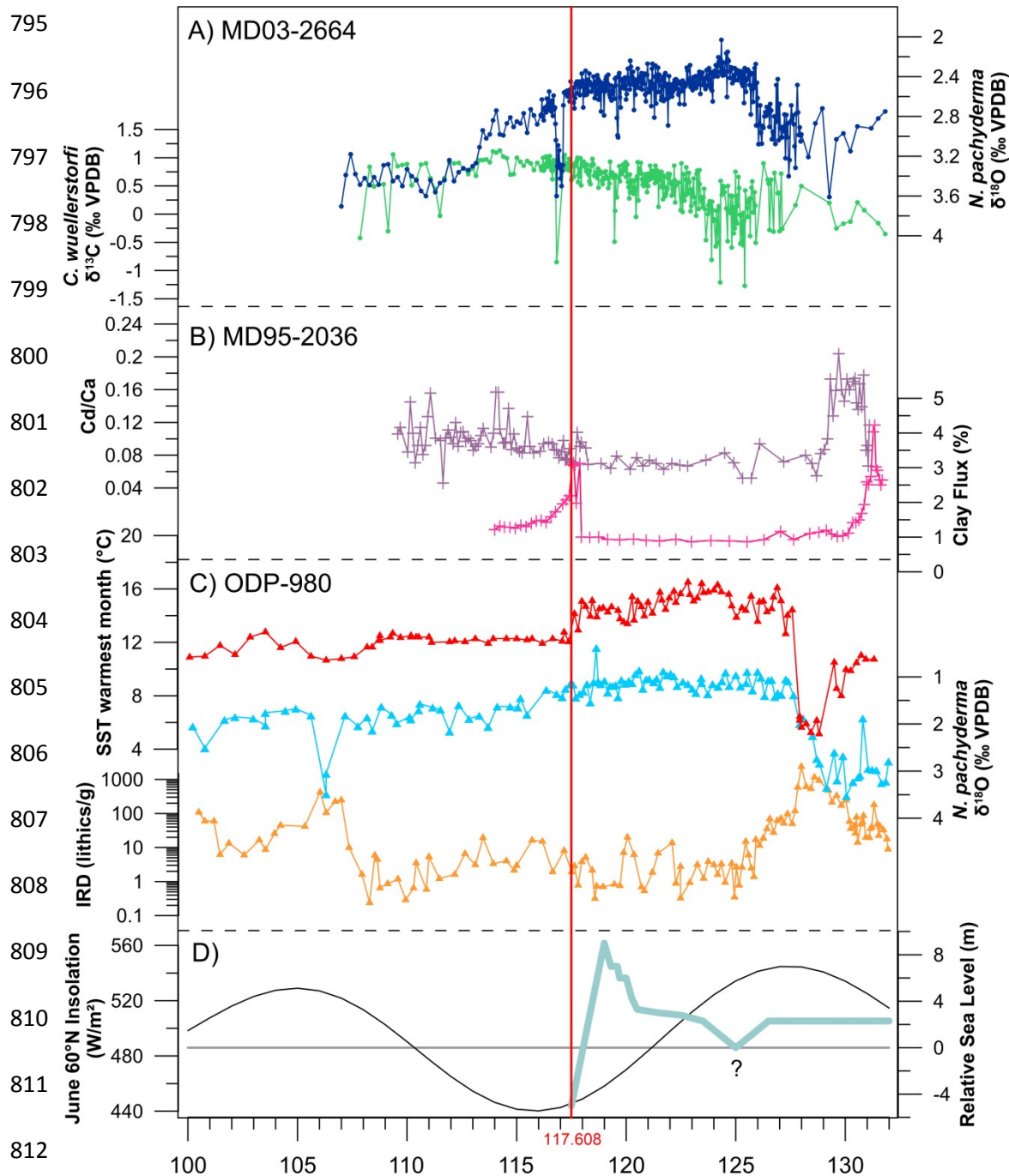


Figure 9: Marine records mentioned in the text. A) Eirik Drift MD03-2664 *N. pachyderma*  $\delta^{18}\text{O}$ , *C. wuellerstorfi*  $\delta^{13}\text{C}$  (Galaasen et al., 2014). B) Bermuda Rise MD95-2036 Cd/Ca and Clay Flux (Adkins et al., 1997). C) ODP-980 Sea Surface Temperature of the warmest month, *N. pachyderma*  $\delta^{18}\text{O}$  and IRD content plotted on a logarithmic scale (Oppo et al., 2006). D) June insolation at 60°N (Berger and Loutre, 1991) and global relative sea level (after Hearty et al., 2007). Red line indicates the timing of the EWT in the Belgian speleothems.



**Table 2: Results of  $^{230}\text{Th}$ - $^{234}\text{U}$  dating**

#	Distance (mm dft) <sup>1</sup>	<sup>238</sup> U (ng g <sup>-1</sup> )		<sup>232</sup> Th ppt		<sup>230</sup> Th / <sup>232</sup> Th (atomic x10-6)		$\delta^{234}$ U (measured) <sup>2</sup>		<sup>230</sup> Th / <sup>238</sup> U (activity)		<sup>230</sup> Th Age (yr) (uncorrected)		<sup>230</sup> Th Age (yr) (corrected)		$\delta^{234}$ U Initial (corrected) <sub>3</sub>		<sup>230</sup> Th Age (yr BP) (corrected) <sup>4</sup>	
RSM-17																			
1	1208	166.7	±0.2	745	±15	3286	±66	290.0	±1.5	0.8911	±0.0019	12012							
												5	±515	120033	±519	407	±2	119970	±519
2	1205	180.7	±0.2	891	±18	2968	±60	285.9	±1.6	0.8875	±0.0014	11999							
												4	±436	119891	±441	401	±2	119825	±441
3	979	233.3	±0.2	789	±16	4348	±88	299.8	±1.2	0.8917	±0.0013	11853							
												1	±360	118462	±363	419	±2	118396	±363
4	929	251	±0	664	±13	5473	±110	285.7	±1.5	0.8774	±0.0015	11770							
												0	±426	117644	±428	398	±2	117578	±428
5	909	213.5	±0.3	713	±14	4399	±89	296.2	±1.5	0.8906	±0.0017	11888							
												6	±471	118817	±473	414	±2	118754	±473
6	882	209	±0	1093	±22	2813	±57	302.7	±1.6	0.8931	±0.0014	11833							
												4	±424	118227	±430	423	±2	118161	±430
7	753	271	±0	914	±18	4398	±88	309.0	±1.5	0.9003	±0.0014	11887							
												1	±415	118802	±417	432	±2	118736	±417
8	727	290.7	±0.5	782	±16	5506	±111	308.8	±1.6	0.8988	±0.0017	11857							
												0	±481	118515	±482	431	±2	118452	±482
9	604	287	±0	1042	±21	4123	±83	332.1	±1.7	0.9086	±0.0015	11681							
												8	±427	116746	±430	462	±2	116680	±430
10	564	502	±1	3078	±62	2462	±49	331.5	±1.5	0.9156	±0.0017	11845							
												7	±458	118335	±465	463	±2	118269	±465
11	548	214.2	±0.3	673	±14	4832	±97	341.3	±1.6	0.9211	±0.0019	11800							
												1	±489	117939	±490	476	±2	117876	±490
12	540	258.3	±0.2	899	±18	4311	±87	326.8	±1.4	0.9104	±0.0012	11809							
												4	±351	118024	±354	456	±2	117958	±354
13	534	420	±1	732	±15	8555	±172	323.7	±1.5	0.9044	±0.0017	11728							
												2	±444	117247	±445	451	±2	117181	±445
14	321	122.1	±0.1	1190	±24	1547	±31	339.1	±1.6	0.9145	±0.0018	11695							
												5	±475	116762	±494	471	±2	116699	±494
15	283	144.5	±0.2	548	±11	3967	±80	348.5	±1.7	0.9130	±0.0019	11510							
												2	±487	115028	±489	482	±2	114965	±489
16	254	147.3	±0.3	966	±19	2288	±46	340.0	±1.9	0.9098	±0.0021	11579							
												2	±543	115662	±550	471	±3	115599	±550
17	136	156	±0	1029	±21	2256	±45	339.5	±1.5	0.9002	±0.0014	11381							
												2	±378	113681	±389	468	±2	113615	±389
Han-8																			
1	167	268.0	±0.3	6391	±12	808	±16	632.6	±1.7	1.1681	±0.0021	12238							
												4	±429	122017	±500	893	±3	121954	±500
2	151	293.1	±0.3	387	±8	14610	±294	639.1	±1.8	1.1705	±0.0018	12192							
												2	±405	121902	±405	901	±3	121839	±405
3	128	289.1	±0.4	241	±5	22950	±463	634.9	±1.8	1.1601	±0.0018	12067							
												1	±391	120658	±391	892	±3	120595	±391
4	124.5	322.9	±0.4	212	±4	29097	±590	631.0	±1.7	1.1558	±0.0018	12044							
													±388	120433	±388	886	±3	120370	±388

												4									
5	104.5	324.5	±0.4	152	±3	40750	±833	641.0	±2.0	1.1581	±0.0020	11951	0	±431	119503	±431	898	±3	119440	±431	
6	83	382.9	±0.5	296	±6	24743	±500	655.7	±2.0	1.1586	±0.0020	11768	1	±419	117669	±419	914	±3	117606	±419	
7	81	281.6	±0.4	557	±11	9635	±194	658.6	±2.0	1.1567	±0.0021	11699	8	±430	116967	±430	916	±3	116904	±430	
8	70.5	281.9	±0.3	227	±5	23785	±485	668.0	±1.9	1.1611	±0.0019	11655	5	±400	116542	±400	928	±3	116479	±400	
9	67	377.7	±0.4	159	±3	44978	±930	652.1	±1.6	1.1470	±0.0019	11619	6	±368	116189	±368	905	±2	116126	±368	
10	55.5	354.8	±0.5	269	±5	24980	±509	659.9	±1.9	1.1490	±0.0022	11554	9	±437	115537	±437	914	±3	115474	±437	
11	52	261.4	±0.3	313	±6	16105	±327	692.0	±2.1	1.1695	±0.0023	11498	1	±444	114963	±444	957	±3	114900	±444	
12	29	149.3	±0.2	828	±17	3487	±70	705.7	±2.1	1.1733	±0.0019	11396	7	±389	113885	±393	973	±3	113822	±393	
13	3	179.4	±0.2	315	±6	11012	±223	730.4	±2.0	1.1741	±0.0020	111285		±371	111260	±372	1000	±3	111197	±372	
Han-9																					
1	668	531.5	±0.6	1693	±34	6077	±122	622.5	±1.5	1.1739	±0.0016	12485	4	±363	124805	±364	885	±2	124740	±364	
	639	475.3	±0.4	6419	±128	1417	±29	606	±3	1.1608	±0.0027	12478	1	±653	124569	±669	862	±4	124506	±669	
	614.6	227.6	±0.2	413	±8	11096	±223	704.0	±1.6	1.2220	±0.0013	12207	5	±304	122049	±305	993	±2	121984	±305	
	581.5	289.7	±0.2	1597	±32	3563	±71	675.2	±1.5	1.1911	±0.0014	12062	5	±304	120542	±310	949	±2	120477	±310	
	554	370.5	±0.3	213	±4	33652	±692	661	±3	1.1759	±0.0029	11993	4	±589	119925	±589	927	±4	119862	±589	
	484.2	390.1	±0.4	1420	±28	5246	±105	637.7	±1.6	1.1583	±0.0015	11997	1	±331	119915	±333	895	±2	119850	±333	
	426	337.7	±0.3	243	±5	26740	±539	656.3	±1.5	1.1679	±0.0013	11917	9	±289	119168	±289	919	±2	119103	±289	
	397	373.4	±0.3	681	±14	10480	±211	650	±2	1.1596	±0.0027	11856	4	±539	118536	±539	908	±3	118473	±539	
	356	636.0	±0.7	1406	±28	8600	±172	648.9	±1.5	1.1533	±0.0014	11766	1	±306	117627	±307	904	±2	117562	±307	
	311	226.6	±0.3	1735	±35	2526	±51	667.0	±3.2	1.1727	±0.0036	11859	6	±727	118481	±731	932	±5	118418	±731	
	305	319.4	±0.3	1412	±28	4254	±86	630.9	±1.7	1.1409	±0.0018	11788	1	±376	117812	±379	880	±3	117746	±379	
	2	297	396.8	±0.4	563	±11	13324	±269	676.9	±2.4	1.1456	±0.0027	11296	4	±512	112942	±512	931	±4	112879	±512
		271	213.5	±0.1	1647	±33	2460	±49	692.3	±1.4	1.1511	±0.0011	11204	5	±237	111930	±251	949	±2	111865	±251
		238.5	239.0	±0.2	208	±4	21967	±446	709.8	±1.6	1.1594	±0.0012	111337		±254	111324	±254	972	±2	111259	±254
		224*	313.4	±0.4	918	±19	6320	±128	685.0	±1.7	1.1234	±0.0019	10857	2	±343	108527	±344	930	±3	108461	±344

3	214	216.2	±0.3	939	±19	4315	±87	691.4	±3.0	1.1365	±0.0035	10988 7	±637	109822	±638	943	±4	109759	±638
	201	158.8	±0.1	386	±8	7695	±155	680.1	±1.5	1.1334	±0.0012	11066 3	±245	110627	±246	929	±2	110562	±246
	<b>189</b>	<b>156.3</b>	<b>±0.1</b>	<b>7024</b>	<b>±14</b> <b>1</b>	<b>415</b>	<b>±8</b>	<b>698.7</b>	<b>±1.7</b>	<b>1.1315</b>	<b>±0.0021</b>	<b>10830</b> <b>4</b>	<b>±363</b>	<b>107631</b>	<b>±598</b>	<b>947</b>	<b>±3</b>	<b>107565</b>	<b>±598</b>
	179.5	179.8	±0.1	3158	±63	1064	±21	711.7	±1.5	1.1341	±0.0011	10730 3	±223	107042	±289	963	±2	106977	±289
4	171	187.0	±0.2	1051	±21	3255	±66	711.7	±4.1	1.1089	±0.0037	10361 5	±671	103531	±673	953	±6	103468	±673
	154*	204.3	±0.2	2749	±55	1339	±27	727.0	±1.5	1.0929	±0.0011	99868	±215	99668	±257	963	±2	99603	±257
	<b>145</b>	<b>187.7</b>	<b>±0.2</b>	<b>2284</b>	<b>±46</b>	<b>1480</b>	<b>±30</b>	<b>713.5</b>	<b>±1.8</b>	<b>1.0927</b>	<b>±0.0016</b>	<b>10113</b> <b>5</b>	<b>±282</b>	<b>100953</b>	<b>±309</b>	<b>949</b>	<b>±2</b>	<b>100887</b>	<b>±309</b>
	125.7*	159.7	±0.1	1709	±34	1673	±34	744.0	±1.6	1.0861	±0.0011	97373	±206	97215	±234	979	±2	97150	±234
	98.7	149.3	±0.2	759	±15	3593	±73	737.3	±4.0	1.1070	±0.0039	10084 7	±664	100772	±666	980	±6	100709	±666
	56*	196.9	±0.1	978	±20	3503	±70	694.6	±1.5	1.0554	±0.0011	97680	±206	97604	±212	915	±2	97539	±212
	34*	234.0	±0.2	359	±7	11228	±226	668.5	±1.6	1.0444	±0.0013	98598	±236	98574	±237	883	±2	98509	±237
5	15.2	240.4	±0.2	531	±11	7898	±161	676.6	±3.1	1.0581	±0.0039	99784	±634	99750	±634	897	±4	99687	±634
	<b>8.5</b>	<b>248.3</b>	<b>±0.2</b>	<b>490</b>	<b>±10</b>	<b>8890</b>	<b>±180</b>	<b>684.8</b>	<b>±1.6</b>	<b>1.0647</b>	<b>±0.0016</b>	<b>99925</b>	<b>±275</b>	<b>99894</b>	<b>±276</b>	<b>908</b>	<b>±2</b>	<b>99828</b>	<b>±276</b>

All errors shown are 2σ uncertainties

U decay constants used:  $\lambda_{238} = 1.55125 \times 10^{-10}$  (Jaffey et al., 1971) and  $\lambda_{234} = 2.82206 \times 10^{-6}$  (Cheng et al., 2013). Th decay constant used:  $\lambda_{230} = 9.1705 \times 10^{-6}$  (Cheng et al., 2013).

Th decay constant used:  $\lambda_{230} = 9.1705 \times 10^{-6}$  (Cheng et al., 2013).

<sup>1</sup> dft = distance from top

<sup>2</sup>  $\delta^{234}\text{U} = ([^{234}\text{U}/^{238}\text{U}]\text{activity} - 1) \times 1000$ .

<sup>3</sup>  $\delta^{234}\text{U}_{\text{initial}}$  was calculated based on <sup>230</sup>Th age (T), i.e.,  $\delta^{234}\text{U}_{\text{initial}} = \delta^{234}\text{U}_{\text{measured}} \times e^{\lambda_{234} \times T}$ .

<sup>4</sup> Corrected <sup>230</sup>Th ages assume the initial <sup>230</sup>Th/<sup>232</sup>Th atomic ratio of  $4.4 \pm 2.2 \times 10^{-6}$ . Those are the values for a material at secular equilibrium, with the bulk earth <sup>232</sup>Th/<sup>238</sup>U value of 3.8.

The errors are arbitrarily assumed to be 50%. B.P. stands for “Before Present” where the “Present” is defined as the year 1950 A.D.

Dashed lines indicate discontinuities in speleothem growth

\* Han-9 dates collected in 2015 (see Vansteenberge et al., 2016)

**Bold** indicates Newly added dates of Han-9

819

820

821

822

823

824

825

826

827

828

829**Table 2: Information about the different tie-points used in Fig. 4**

<b>Tie point</b>	<b>Han-8 dft (mm)</b>	<b>Han-8 Age (ka)</b>	<b>Han-8 Error range (ka)</b>		<b>Han-9 dft (mm)</b>	<b>Han-9 Age (ka)</b>	<b>Han-9 Error range (ka)</b>		<b>Age Difference Han-8/Han-9 (ka)</b>	<b>Tuned Age (ka)</b>	<b>Tuned Age Error (ka)</b>
1	170	122.284	122.764	121.860	611	121.920	122.228	121.576	0.364	<b>122.102</b>	<b>±0.389</b>
2	122	120.280	120.580	120.012	466	119.519	119.885	119.260	0.761	<b>119.900</b>	<b>±0.298</b>
3	105	119.294	119.812	118.970	438	119.208	119.537	118.979	0.086	<b>119.251</b>	<b>±0.35</b>
4	93	118.487	119.338	118.157	389.5	118.399	118.943	117.992	0.088	<b>118.443</b>	<b>±0.533</b>
5	88.75	118.157	118.829	117.843	371.5	117.969	118.715	117.639	0.188	<b>118.063</b>	<b>±0.515</b>
6	81.5	117.675	118.088	117.304	304.5	117.339	117.739	116.536	0.336	<b>117.507</b>	<b>±0.497</b>
7	4	111.613	112.113	111.110	282	112.255	112.580	111.924	-0.642	<b>111.934</b>	<b>±0.415</b>
8	1	111.392	111.914	110.860	260	111.693	111.874	111.480	-0.301	<b>111.543</b>	<b>±0.362</b>

830



## 832References

- 833Adkins, J.F., Boyle, E.A., Keigwin, L. and Cortijo, E. (1997) Variability of the North Atlantic thermohaline  
834circulation during the last interglacial period. *Nature*, **390**, 154-156.
- 835Allan, M., Fagel, N., Van Rampelbergh, M., Baldini, J., Riotte, J., Cheng, H., Edwards, R.L., Gillikin, D.,  
836Quinif, Y. and Verheyden, S. (2015) Lead concentrations and isotope ratios in speleothems as proxies for  
837atmospheric metal pollution since the industrial revolution. *Chemical Geology*, **401**, 140-150.
- 838Allen, J.R.M. and Huntley, B. (2009) Last Interglacial palaeovegetation, palaeoenvironments and  
839chronology: a new record from Lago Grande di Monticchio, southern Italy. *Quaternary Science Reviews*,  
840**28**, 1521-1538.
- 841Bar-Matthews, M., Ayalon, A., Gilmour, M., Matthews, A. and Hawkesworth, C.J. (2003) Sea-land  
842oxygen isotopic relationships from planktonic foraminifera and speleothems in the Eastern  
843Mediterranean region and their implication for paleorainfall during interglacial intervals. *Geochimica et*  
844*Cosmochimica Acta*, **67**, 3181-3199.
- 845Bauch, H.A., Kandiano, E.S., Helmke, J., Andersen, N., Rosell-Mele, A. and Erlenkeuser, H. (2011)  
846Climatic bisection of the last interglacial warm period in the Polar North Atlantic. *Quaternary Science*  
847*Reviews*, **30**, 1813-1818.
- 848Bazin, L., Landais, A., Lemieux-Dudon, B., Kele, H.T.M., Veres, D., Parrenin, F., Martinerie, P., Ritz, C.,  
849Capron, E., Lipenkov, V., Loutre, M.F., Raynaud, D., Vinther, B., Svensson, A., Rasmussen, S.O., Severi,  
850M., Blunier, T., Leuenberger, M., Fischer, H., Masson-Delmotte, V., Chappellaz, J. and Wolff, E. (2013) An  
851optimized multi-proxy, multi-site Antarctic ice and gas orbital chronology (AICC2012): 120-800 ka.  
852*Climate of the Past*, **9**, 1715-1731.
- 853Berger, A., Crucifix, M., Hodell, D.A., Mangili, C., McManus, J.F., Otto-Bliesner, B., Pol, K., Raynaud, D.,  
854Skinner, L.C., Tzedakis, P.C., Wolff, E.W., Yin, Q.Z., Abe-Ouchi, A., Barbante, C., Brovkin, V., Cacho, I.,  
855Capron, E., Ferretti, P., Ganopolski, A., Grimalt, J.O., Honisch, B., Kawamura, K., Landais, A., Margari,  
856V., Martrat, B., Masson-Delmotte, V., Mokeddem, Z., Parrenin, F., Prokopenko, A.A., Rashid, H., Schulz,  
857M., Riveiros, N.V. and Past Interglacials Working Grp, P.A.G. (2016) Interglacials of the last  
858800,000years. *Reviews of Geophysics*, **54**, 162-219.
- 859Berger, A. and Loutre, M.F. (1991) INSOLATION VALUES FOR THE CLIMATE OF THE LAST 10000000 YEARS.  
860*Quaternary Science Reviews*, **10**, 297-317.
- 861Blanchon, P., Eisenhauer, A., Fietzke, J. and Liebetrau, V. (2009) Rapid sea-level rise and reef back-  
862stepping at the close of the last interglacial highstand. *Nature*, **458**, 881-U6.
- 863Boch, R., Cheng, H., Spotl, C., Edwards, R.L., Wang, X. and Hauselmann, P. (2011) NALPS: a precisely  
864dated European climate record 120-60 ka. *Climate of the Past*, **7**, 1247-1259.
- 865Bonniver, I. (2010) Hydrogéologie du Massif de Boine. In: *EcoKarst*, **81**, pp. 1-4, La Hulpe.
- 866Borsato, A., Frisia, S., Fairchild, I.J., Somogyi, A. and Susini, J. (2007) Trace element distribution in  
867annual stalagmite laminae mapped by micrometer-resolution X-ray fluorescence: Implications for  
868incorporation of environmentally significant species. *Geochimica Et Cosmochimica Acta*, **71**, 1494-1512.
- 869Bourdin, C., Douville, E. and Genty, D. (2011) Alkaline-earth metal and rare-earth element incorporation  
870control by ionic radius and growth rate on a stalagmite from the Chauvet Cave, Southeastern France.  
871*Chemical Geology*, **290**, 1-11.
- 872Brauer, A., Allen, J.R.M., Mingram, J., Dulski, P., Wulf, S. and Huntley, B. (2007) Evidence for last  
873interglacial chronology and environmental change from Southern Europe. *Proceedings of the National*  
874*Academy of Sciences of the United States of America*, **104**, 450-455.
- 875Breitenbach, S.F.M., Rehfeld, K., Goswami, B., Baldini, J.U.L., Ridley, H.E., Kennett, D.J., Prufer, K.M.,  
876Aquino, V.V., Asmerom, Y., Polyak, V.J., Cheng, H., Kurths, J. and Marwan, N. (2012) CONstructing Proxy  
877Records from Age models (COPRA). *Climate of the Past*, **8**, 1765-1779.

878Brewer, S., Guiot, J., Sanchez-Goni, M.F. and Klotz, S. (2008) The climate in Europe during the Eemian: a  
879multi-method approach using pollen data. *Quaternary Science Reviews*, **27**, 2303-2315.

880Capron, E., Govin, A., Stone, E.J., Masson-Delmotte, V., Mulitza, S., Otto-Bliesner, B., Rasmussen, T.L.,  
881Sime, L.C., Waelbroeck, C. and Wolff, E.W. (2014) Temporal and spatial structure of multi-millennial  
882temperature changes at high latitudes during the Last Interglacial. *Quaternary Science Reviews*, **103**, 116-  
883133.

884Capron, E., Landais, A., Chappellaz, J., Buiron, D., Fischer, H., Johnsen, S.J., Jouzel, J., Leuenberger, M.,  
885Masson-Delmotte, V. and Stocker, T.F. (2012) A global picture of the first abrupt climatic event occurring  
886during the last glacial inception. *Geophysical Research Letters*, **39**.

887Capron, E., Landais, A., Chappellaz, J., Schilt, A., Buiron, D., Dahl-Jensen, D., Johnsen, S.J., Jouzel, J.,  
888Lemieux-Dudon, B., Louergue, L., Leuenberger, M., Masson-Delmotte, V., Meyer, H., Oerter, H. and  
889Stenni, B. (2010) Millennial and sub-millennial scale climatic variations recorded in polar ice cores over  
890the last glacial period. *Climate of the Past*, **6**, 345-365.

891Chapman, M.R. and Shackleton, N.J. (1999) Global ice-volume fluctuations, North Atlantic ice-rafting  
892events, and deep-ocean circulation changes between 130 and 70 ka. *Geology*, **27**, 795-798.

893Cheng, H., Edwards, R.L., Chuan-Chou, S., Polyak, V.J., Asmerom, Y., Woodhead, J., Hellstrom, J.,  
894Yongjin, W., Xinggong, K., Spotl, C., Xianfeng, W. and Alexander, E.C., Jr. (2013) Improvements in 230Th  
895dating, 230Th and 234U half-life values, and U-Th isotopic measurements by multi-collector inductively  
896coupled plasma mass spectrometry. *Earth and Planetary Science Letters*, **371-372**, 82-91.

897Coen, M. (1970) Stratigraphie du Frasnien de la Grotte de Remouchamps. *Annales de la Société*  
898*Géologique de Belgique*, **93**, 73-79.

899Couchoud, I., Genty, D., Hoffmann, D., Drysdale, R. and Blamart, D. (2009) Millennial-scale climate  
900variability during the Last Interglacial recorded in a speleothem from south-western France. *Quaternary*  
901*Science Reviews*, **28**, 3263-3274.

902Dahl-Jensen, D., Albert, M.R., Aldahan, A., Azuma, N., Balslev-Clausen, D., Baumgartner, M., Berggren,  
903A.M., Bigler, M., Binder, T., Blunier, T., Bourgeois, J.C., Brook, E.J., Buchardt, S.L., Buizert, C., Capron, E.,  
904Chappellaz, J., Chung, J., Clausen, H.B., Cvijanovic, I., Davies, S.M., Ditlevsen, P., Eicher, O., Fischer, H.,  
905Fisher, D.A., Fleet, L.G., Gfeller, G., Gkinis, V., Gogineni, S., Goto-Azuma, K., Grinsted, A.,  
906Gudlaugsdottir, H., Guillevic, M., Hansen, S.B., Hansson, M., Hirabayashi, M., Hong, S., Hur, S.D.,  
907Huybrechts, P., Hvidberg, C.S., Iizuka, Y., Jenk, T., Johnsen, S.J., Jones, T.R., Jouzel, J., Karlsson, N.B.,  
908Kawamura, K., Keegan, K., Kettner, E., Kipfstuhl, S., Kjaer, H.A., Koutnik, M., Kuramoto, T., Kohler, P.,  
909Laepple, T., Landais, A., Langen, P.L., Larsen, L.B., Leuenberger, D., Leuenberger, M., Leuschen, C., Li, J.,  
910Lipenkov, V., Martinerie, P., Maselli, O.J., Masson-Delmotte, V., McConnell, J.R., Miller, H., Mini, O.,  
911Miyamoto, A., Montagnat-Rentier, M., Mulvaney, R., Muscheler, R., Orsi, A.J., Paden, J., Panton, C.,  
912Pattyn, F., Petit, J.R., Pol, K., Popp, T., Possnert, G., Prie, F., Prokopiou, M., Quiquet, A., Rasmussen,  
913S.O., Raynaud, D., Ren, J., Reutenauer, C., Ritz, C., Rockmann, T., Rosen, J.L., Rubino, M., Rybak, O.,  
914Samyn, D., Sapart, C.J., Schilt, A., Schmidt, A.M.Z., Schwander, J., Schupbach, S., Seierstad, I.,  
915Severinghaus, J.P., Sheldon, S., Simonsen, S.B., Sjolte, J., Solgaard, A.M., Sowers, T., Sperlich, P., Steen-  
916Larsen, H.C., Steffen, K., Steffensen, J.P., Steinhage, D., Stocker, T.F., Stowasser, C., Sturevik, A.S.,  
917Sturges, W.T., Sveinbjornsdottir, A., Svensson, A., Tison, J.L., Uetake, J., Vallelonga, P., van de Wal,  
918R.S.W., van der Wel, G., Vaughn, B.H., Vinther, B., Waddington, E., Wegner, A., Weikusat, I., White,  
919J.W.C., Wilhelms, F., Winstrup, M., Witrant, E., Wolff, E.W., Xiao, C., Zheng, J. and Community, N. (2013)  
920Eemian interglacial reconstructed from a Greenland folded ice core. *Nature*, **493**, 489-494.

921Day, C.C. and Henderson, G.M. (2013) Controls on trace-element partitioning in cave-analogue calcite.  
922*Geochimica Et Cosmochimica Acta*, **120**, 612-627.

923Demeny, A., Kern, Z., Czippon, G., Nemeth, A., Leel-Ossy, S., Siklosy, Z., Lin, K., Hu, H.M., Shen, C.C.,  
924Vennemann, T.W. and Haszpra, L. (2017) Stable isotope compositions of speleothems from the last  
925interglacial - Spatial patterns of climate fluctuations in Europe. *Quaternary Science Reviews*, **161**, 68-80.

926Dorale, J.A. and Liu, Z.H. (2009) LIMITATIONS OF HENDY TEST CRITERIA IN JUDGING THE PALEOCLIMATIC  
927SUITABILITY OF SPELEOTHEMS AND THE NEED FOR REPLICATION. *Journal of Cave and Karst Studies*, **71**,  
92873-80.

929Drysedale, R.N., Hellstrom, J.C., Zanchetta, G., Fallick, A.E., Sánchez Goñi, M.F., Couchoud, I., McDonald,  
930J., Maas, R., Lohmann, G. and Isola, I. (2009) Evidence for Obliquity Forcing of Glacial Termination II.  
931*Science*, **325**, 1527-1531.

932Drysedale, R.N., Zanchetta, G., Hellstrom, J.C., Fallick, A.E., McDonald, J. and Cartwright, I. (2007)  
933Stalagmite evidence for the precise timing of North Atlantic cold events during the early last glacial.  
934*Geology*, **35**, 77-80.

935Drysedale, R.N., Zanchetta, G., Hellstrom, J.C., Fallick, A.E. and Zhao, J.X. (2005) Stalagmite evidence for  
936the onset of the Last Interglacial in southern Europe at 129 +/- 1 ka. *Geophysical Research Letters*, **32**.  
937Dutton, A., Carlson, A.E., Long, A.J., Milne, G.A., Clark, P.U., DeConto, R., Horton, B.P., Rahmstorf, S.  
938and Raymo, M.E. (2015) Sea-level rise due to polar ice-sheet mass loss during past warm periods.  
939*Science*, **349**.

940Dutton, A. and Lambeck, K. (2012) Ice Volume and Sea Level During the Last Interglacial. *Science*, **337**,  
941216-219.

942Edwards, R.L., Chen, J.H., Ku, T.L. and Wasserburg, G.J. (1987) Precise Timing of the Last Interglacial  
943Period from Mass Spectrometric Determination of Thorium-230 in Corals. *Science*, **236**, 1547-1553.

944Ek, C. (1970) Carte Géologique de la Grotte de Remouchamps (Belgique). *Annales de la Société*  
945*Géologique de Belgique*, **93**, 287-292.

946Fairchild, I.J. and Baker, A. (2012) *Speleothem Science: from process to past environments*. Wiley-  
947Blackwell.

948Fairchild, I.J., Baker, A., Borsato, A., Frisia, S., Hinton, R.W., McDermott, F. and Tooth, A.F. (2001)  
949Annual to sub-annual resolution of multiple trace-element trends in speleothems. *Journal of the*  
950*Geological Society*, **158**, 831-841.

951Fairchild, I.J., Borsato, A., Tooth, A.F., Frisia, S., Hawkesworth, C.J., Huang, Y.M., McDermott, F. and  
952Spiro, B. (2000) Controls on trace element (Sr-Mg) compositions of carbonate cave waters: implications  
953for speleothem climatic records. *Chemical Geology*, **166**, 255-269.

954Fairchild, I.J. and Treble, P.C. (2009) Trace elements in speleothems as recorders of environmental  
955change. *Quaternary Science Reviews*, **28**, 449-468.

956Friedman, I., O'Neil, J. and Cebula, G. (1982) Two New Carbonate Stable-Isotope Standards.  
957*Geostandards Newsletter*, **6**, 11-12.

958Frisia, S., Borsato, A., Drysdale, R.N., Paul, B., Greig, A. and Cotte, M. (2012) A re-evaluation of the  
959palaeoclimatic significance of phosphorus variability in speleothems revealed by high-resolution  
960synchrotron micro XRF mapping. *Climate of the Past*, **8**, 2039-2051.

961Fronval, T., Jansen, E., Hafliðason, H. and Sejrup, H.P. (1998) Variability in surface and deep water  
962conditions in the Nordic Seas during the last interglacial period. *Quaternary Science Reviews*, **17**, 963-  
963985.

964Galaasen, E.V., Ninnemann, U.S., Irvali, N., Kleiven, H.F., Rosenthal, Y., Kissel, C. and Hodell, D.A. (2014)  
965Rapid Reductions in North Atlantic Deep Water During the Peak of the Last Interglacial Period. *Science*,  
966**343**, 1129-1132.

967Genty, D. and Deflandre, G. (1998) Drip flow variations under a stalactite of the Pere Noel cave  
968(Belgium). Evidence of seasonal variations and air pressure constraints. *Journal of Hydrology*, **211**, 208-  
969232.

970Genty, D., Verheyden, S. and Wainer, K. (2013) Speleothem records over the Last Interglacial, **21**, pp. 24-  
97125. PAGES.

972Gewelt, M. (1985) Cinétique du concrétionnement dans quelques grottes Belges: apport des datations <sup>14</sup>C  
973et <sup>230</sup>Th/<sup>234</sup>U. *Annales de la Société Géologique de Belgique*, **108**, 267-273.



974 Govin, A., Capron, E., Tzedakis, P.C., Verheyden, S., Ghaleb, B., Hillaire-Marcel, C., St-Onge, G., Stoner,  
975 J.S., Bassinot, F., Bazin, L., Blunier, T., Combourieu-Nebout, N., El Ouahabi, A., Genty, D., Gersonde, R.,  
976 Jimenez-Amat, P., Landais, A., Martrat, B., Masson-Delmotte, V., Parrenin, F., Seidenkrantz, M.S.,  
977 Veres, D., Waelbroeck, C. and Zahn, R. (2015) Sequence of events from the onset to the demise of the  
978 Last Interglacial: Evaluating strengths and limitations of chronologies used in climatic archives.  
979 *Quaternary Science Reviews*, **129**, 1-36.

980 Granoszewski, W. (2003) Late Pleistocene vegetation history and climatic changes at Horszki Duze,  
981 eastern Poland: a palaeobotanical study. *Acta Palaeobotanica*, **4**, 3-95.

982 Hai, C., Edwards, R.L., Chuan-Chou, S., Polyak, V.J., Asmerom, Y., Woodhead, J., Hellstrom, J., Yongjin,  
983 W., Xingong, K., Spotl, C., Xianfeng, W. and Alexander, E.C., Jr. (2013) Improvements in <sup>230</sup>Th dating,  
984 <sup>230</sup>Th and <sup>234</sup>U half-life values, and U-Th isotopic measurements by multi-collector inductively coupled  
985 plasma mass spectrometry. *Earth and Planetary Science Letters*, **371-372**, 82-91.

986 Hartland, A., Fairchild, I.J., Lead, J.R., Borsato, A., Baker, A., Frisia, S. and Baalousha, M. (2012) From  
987 soil to cave: Transport of trace metals by natural organic matter in karst dripwaters. *Chemical Geology*,  
988 **304**, 68-82.

989 Hearty, P.J., Hollin, J.T., Neumann, A.C., O'Leary, M.J. and McCulloch, M. (2007) Global sea-level  
990 fluctuations during the Last Interglaciation (MIS 5e). *Quaternary Science Reviews*, **26**, 2090-2112.

991 Helmens, K.F. (2014) The Last Interglacial Glacial cycle (MIS 5-2) re-examined based on long proxy  
992 records from central and northern Europe. *Quaternary Science Reviews*, **86**, 115-143.

993 Hendy, C.H. (1971) Isotopic geochemistry of speleothems: calculation of effects of different modes of  
994 formation on isotopic composition of speleothems and their applicability as paleoclimatic indicators.  
995 *Geochimica Et Cosmochimica Acta*, **35**, 801-&.

996 Hodell, D.A., Minth, E.K., Curtis, J.H., McCave, I.N., Hall, I.R., Channell, J.E.T. and Xuan, C. (2009)  
997 Surface and deep-water hydrography on Gardar Drift (Iceland Basin) during the last interglacial period.  
998 *Earth and Planetary Science Letters*, **288**, 10-19.

999 Huang, H.M., Fairchild, I.J., Borsato, A., Frisia, S., Cassidy, N.J., McDermott, F. and Hawkesworth, C.J.  
1000 (2001) Seasonal variations in Sr, Mg and P in modern speleothems (Grotta di Ernesto, Italy). *Chemical*  
1001 *Geology*, **175**, 429-448.

1002 Irvali, N., Ninnemann, U.S., Galaasen, E.V., Rosenthal, Y., Kroon, D., Oppo, D.W., Kleiven, H.F., Darling,  
1003 K.F. and Kissel, C. (2012) Rapid switches in subpolar North Atlantic hydrography and climate during the  
1004 Last Interglacial (MIS 5e). *Paleoceanography*, **27**, 16.

1005 Irvali, N., Ninnemann, U.S., Kleiven, H.F., Galaasen, E.V., Morley, A. and Rosenthal, Y. (2016) Evidence  
1006 for regional cooling, frontal advances, and East Greenland Ice Sheet changes during the demise of the  
1007 last interglacial. *Quaternary Science Reviews*, **150**, 184-199.

1008 Jouzel, J., Masson-Delmotte, V., Cattani, O., Dreyfus, G., Falourd, S., Hoffmann, G., Minster, B., Nouet,  
1009 J., Barnola, J.M., Chappellaz, J., Fischer, H., Gallet, J.C., Johnsen, S., Leuenberger, M., Loulergue, L.,  
1010 Luethi, D., Oerter, H., Parrenin, F., Raisbeck, G., Raynaud, D., Schilt, A., Schwander, J., Selmo, E.,  
1011 Souchez, R., Spahni, R., Stauffer, B., Steffensen, J.P., Stenni, B., Stocker, T.F., Tison, J.L., Werner, M. and  
1012 Wolff, E.W. (2007) Orbital and millennial Antarctic climate variability over the past 800,000 years.  
1013 *Science*, **317**, 793-796.

1014 Kukla, G., McManus, J.F., Rousseau, D.D. and Chuine, I. (1997) How long and how stable was the last  
1015 interglacial? *Quaternary Science Reviews*, **16**, 605-612.

1016 Kukla, G.J., Bender, M.L., de Beaulieu, J.L., Bond, G., Broecker, W.S., Cleveringa, P., Gavin, J.E., Herbert,  
1017 T.D., Imbrie, J., Jouzel, J., Keigwin, L.D., Knudsen, K.L., McManus, J.F., Merkt, J., Muhs, D.R., Muller, H.,  
1018 Poore, R.Z., Porter, S.C., Seret, G., Shackleton, N.J., Turner, C., Tzedakis, P.C. and Winograd, I.J. (2002)  
1019 Last interglacial climates. *Quaternary Research*, **58**, 2-13.

1020Lazareth, C.E., Putten, E.V., André, L. and Dehairs, F. (2003) High-resolution trace element profiles in  
1021shells of the mangrove bivalve *Isognomon ehippium*: a record of environmental spatio-temporal  
1022variations? *Estuarine, Coastal and Shelf Science*, **57**, 1103-1114.

1023Lehman, S.J., Sachs, J.P., Crotwell, A.M., Keigwin, L.D. and Boyle, E.A. (2002) Relation of subtropical  
1024Atlantic temperature, high-latitude ice rafting, deep water formation, and European climate 130,000-  
102560,000 years ago. *Quaternary Science Reviews*, **21**, 1917-1924.

1026Lorens, R.B. (1981) Sr, Cd, Mn and Co distribution coefficients in calcite as a function of calcite  
1027precipitation rate. *Geochimica et Cosmochimica Acta*, **45**, 553-561.

1028Loutre, M.F., Fichet, T., Goosse, H., Huybrechts, P., Goelzer, H. and Capron, E. (2014) Factors  
1029controlling the last interglacial climate as simulated by LOVECLIM1.3. *Clim. Past*, **10**, 1541-1565.

1030Masson-Delmotte, V., Schulz, M., Abe-Ouchi, A., Beer, J., Ganopolski, A., González Rouco, J.F., Jansen,  
1031E., Lambeck, K., Luterbacher, J., Naish, T., Osborn, T., Otto-Bliesner, B., Quinn, T., Ramesh, R., Rojas, M.,  
1032Shao, X. and Timmermann, A. (2013) Information from Paleoclimate Archives. In: *Climate Change 2013:*  
1033*The Physical Science Basis. Contribution*

1034*of Working Group I to the Fifth Assessment Report of the Intergovernmental Panel on Climate Change*  
1035(Eds Stocker, T.F., D. Qin, G.-K. Plattner, M. Tignor, S.K. Allen, J. Boschung, A. Nauels, Y. Xia, V. Bex and P.M.  
1036Midgley). Cambridge University Press, Cambridge, United Kingdom and New York, NY, USA.

1037Meyer, M.C., Spotl, C. and Mangini, A. (2008) The demise of the Last Interglacial recorded in isotopically  
1038dated speleothems from the Alps. *Quaternary Science Reviews*, **27**, 476-496.

1039Moseley, G.E., Smart, P.L., Richards, D.A. and Hoffmann, D.L. (2013) Speleothem constraints on marine  
1040isotope stage (MIS) 5 relative sea levels, Yucatan Peninsula, Mexico. *Journal of Quaternary Science*, **28**,  
1041293-300.

1042Moseley, G.E., Spötl, C., Cheng, H., Boch, R., Min, A. and Edwards, R.L. (2015) Termination-II  
1043interstadial/stadial climate change recorded in two stalagmites from the north European Alps.  
1044*Quaternary Science Reviews*, **127**, 229-239.

1045Müller, U.C., Sánchez Goñi, M.F., Sirocko, F., Claussen, M., Sánchez Goñi, M.F. and Litt, T. (2007) 19.  
1046Vegetation dynamics in southern Germany during marine isotope stage 5 (~ 130 to 70 kyr ago). In:  
1047*Developments in Quaternary Sciences*, **7**, pp. 277-287. Elsevier.

1048Nehme, C., Verheyden, S., Noble, S.R., Farrant, A.R., Sahy, D., Hellstrom, J., Delannoy, J.J. and Claeys, P.  
1049(2015) Reconstruction of MIS 5 climate in the central Levant using a stalagmite from Kanaan Cave,  
1050Lebanon. *Climate of the Past*, **11**, 1785-1799.

1051NGRIP members (2004) High-resolution record of Northern Hemisphere climate extending into the last  
1052interglacial period. *Nature*, **431**, 147-151.

1053O'Leary, M.J., Hearty, P.J., Thompson, W.G., Raymo, M.E., Mitrovica, J.X. and Webster, J.M. (2013) Ice  
1054sheet collapse following a prolonged period of stable sea level during the last interglacial. *Nature*  
1055*Geoscience*, **6**, 796-800.

1056Oppo, D.W., McManus, J.F. and Cullen, J.L. (2006) Evolution and demise of the Last Interglacial warmth  
1057in the subpolar North Atlantic. *Quaternary Science Reviews*, **25**, 3268-3277.

1058Otto-Bliesner, B.L., Rosenbloom, N., Stone, E.J., McKay, N.P., Lunt, D.J., Brady, E.C. and Overpeck, J.T.  
1059(2013) How warm was the last interglacial? New model-data comparisons. *Philosophical Transactions of*  
1060*the Royal Society a-Mathematical Physical and Engineering Sciences*, **371**.

1061Otvos, E.G. (2015) The Last Interglacial Stage: Definitions and marine highstand, North America and  
1062Eurasia. *Quaternary International*, **383**, 158-173.

1063Peel, M.C., Finlayson, B.L. and McMahon, T.A. (2007) Updated world map of the Koppen-Geiger climate  
1064classification. *Hydrology and Earth System Sciences*, **11**, 1633-1644.

1065Pingitore, N.E. and Eastman, M.P. (1986) THE COPRECIPITATION OF SR-2+ WITH CALCITE AT 25-  
1066DEGREES-C AND 1-ATM. *Geochimica Et Cosmochimica Acta*, **50**, 2195-2203.

1067Pol, K., Masson-Delmotte, V., Cattani, O., Debret, M., Falourd, S., Jouzel, J., Landais, A., Minster, B.,  
1068Mudelsee, M., Schulz, M. and Stenni, B. (2014) Climate variability features of the last interglacial in the  
1069East Antarctic EPICA Dome C ice core. *Geophysical Research Letters*, **41**, 4004-4012.

1070Quinif, Y. (2006) Complex stratigraphic sequences in Belgian caves: correlation with climate changes  
1071during the Middle, the Upper Pleistocene and the Holocene. *Geologica Belgica*, **9**, 231-244.

1072Quinif, Y. and Bastin, B. (1994) Datation Uranium/Thorium et Analyse Pollinique d'une Séquence  
1073Stalagmitique du Stade 5 (Galerie des Verviétois, Grotte de Han-sur-Lesse, Belgique). *Comptes Rendus de*  
1074*l'Académie des Sciences*, **318**, 211-217.

1075R Core Team (2013) R: a language and environment for statistical computing. R Foundation for Statistical  
1076Computing, Vienna, Austria.

1077Rasmussen, S.O., Bigler, M., Blockley, S.P., Blunier, T., Buchardt, S.L., Clausen, H.B., Cvijanovic, I., Dahl-  
1078Jensen, D., Johnsen, S.J., Fischer, H., Gkinis, V., Guillevic, M., Hoek, W.Z., Lowe, J.J., Pedro, J.B., Popp,  
1079T., Seierstad, I.K., Steffensen, J.P., Svensson, A.M., Vallelonga, P., Vinther, B.M., Walker, M.J.C.,  
1080Wheatley, J.J. and Winstrup, M. (2014) A stratigraphic framework for abrupt climatic changes during the  
1081Last Glacial period based on three synchronized Greenland ice-core records: refining and extending the  
1082INTIMATE event stratigraphy. *Quaternary Science Reviews*, **106**, 14-28.

1083Regattieri, E., Zanchetta, G., Drysdale, R.N., Isola, I., Woodhead, J.D., Hellstrom, J.C., Giaccio, B., Greig,  
1084A., Baneschi, I. and Dotsika, E. (2016) Environmental variability between the penultimate deglaciation  
1085and the mid Eemian: Insights from Tana che Urla (central Italy) speleothem trace element record.  
1086*Quaternary Science Reviews*, **152**, 80-92.

1087Roberts, M.S., Smart, P.L. and Baker, A. (1998) Annual trace element variations in a Holocene  
1088speleothem. *Earth and Planetary Science Letters*, **154**, 237-246.

1089Scholz, D. and Hoffmann, D.L. (2011) StalAge - An algorithm designed for construction of speleothem  
1090age models. *Quaternary Geochronology*, **6**, 369-382.

1091Scholz, D., Hoffmann, D.L., Hellstrom, J. and Bronk Ramsey, C. (2012) A comparison of different  
1092methods for speleothem age modelling. *Quaternary Geochronology*, **14**, 94-104.

1093Shackleton, N.J. (1969) LAST INTERGLACIAL IN MARINE AND TERRESTRIAL RECORDS. *Proceedings of the*  
1094*Royal Society Series B-Biological Sciences*, **174**, 135-+.

1095Shackleton, N.J., Sanchez-Goni, M.F., Paillet, D. and Lancelot, Y. (2003) Marine Isotope Substage 5e and  
1096the Eemian interglacial. *Global and Planetary Change*, **36**, 151-155.

1097Shen, C.-C., Wu, C.-C., Cheng, H., Lawrence Edwards, R., Hsieh, Y.-T., Gallet, S., Chang, C.-C., Li, T.-Y.,  
1098Lam, D.D., Kano, A., Hori, M. and Spötl, C. (2012) High-precision and high-resolution carbonate  $^{230}\text{Th}$   
1099dating by MC-ICP-MS with SEM protocols. *Geochimica et Cosmochimica Acta*, **99**, 71-86.

1100Sirocko, F., Seelos, K., Schaber, K., Rein, B., Dreher, F., Diehl, M., Lehne, R., Jager, K., Krbetschek, M.  
1101and Degering, D. (2005) A late Eemian aridity pulse in central Europe during the last glacial inception.  
1102*Nature*, **436**, 833-836.

1103Sivan, D., Sisma-Ventura, G., Greenbaum, N., Bialik, O.M., Williams, F.H., Tamisiea, M.E., Rohling, E.J.,  
1104Frumkin, A., Avnaim-Katav, S., Shtienberg, G. and Stein, M. (2016) Eastern Mediterranean sea levels  
1105through the last interglacial from a coastal-marine sequence in northern Israel. *Quaternary Science*  
1106*Reviews*, **145**, 204-225.

1107Sánchez Goñi, M.F., Eynaud, F., Turon, J.L. and Shackleton, N.J. (1999) High resolution palynological  
1108record off the Iberian margin: direct land-sea correlation for the Last Interglacial complex. *Earth and*  
1109*Planetary Science Letters*, **171**, 123-137.

1110Timperman, M. (1989) *La Grotte de Han: Au Fil de Siècles*, Gembloux, 66 pp.

1111Treble, P., Shelley, J.M.G. and Chappell, J. (2003) Comparison of high resolution sub-annual records of  
1112trace elements in a modern (1911-1992) speleothem with instrumental climate data from southwest  
1113Australia. *Earth and Planetary Science Letters*, **216**, 141-153.

1114Tzedakis, C., Capron, E., de Vernal, A., Otto-Bliesner, B. and Wolff, E. (2015) New PAGES-PMIP working  
1115group on Quaternary Interglacials (QUIGS) *PAGES Magazine*, **23**, 83.

1116Tzedakis, P.C., Frogley, M.R. and Heaton, T.H.E. (2003) Last Interglacial conditions in southern Europe:  
1117evidence from Ioannina, northwest Greece. *Global and Planetary Change*, **36**, 157-170.

1118Van Rampelbergh, M., Verheyden, S., Allan, M., Quinif, Y., Cheng, H., Edwards, L.R., Keppens, E. and  
1119Claeys, P. (2015) A 500-year seasonally resolved  $\delta^{18}\text{O}$  and  $\delta^{13}\text{C}$ , layer thickness and calcite aspect  
1120record from a speleothem deposited in the Han-sur-Lesse cave, Belgium. *Clim. Past*, **11**, 789-802.

1121Van Rampelbergh, M., Verheyden, S., Allan, M., Quinif, Y., Keppens, E. and Claeys, P. (2014) Monitoring  
1122of a fast-growing speleothem site from the Han-sur-Lesse cave, Belgium, indicates equilibrium deposition  
1123of the seasonal  $\delta^{18}\text{O}$  and  $\delta^{13}\text{C}$  signals in the calcite. *Climate of the Past*, **10**, 1871-1885.

1124Vansteenberghe, S., Verheyden, S., Cheng, H., Edwards, R.L., Keppens, E. and Claeys, P. (2016)  
1125Paleoclimate in continental northwestern Europe during the Eemian and early Weichselian (125-97ka):  
1126insights from a Belgian speleothem. *Climate of the Past*, **12**, 1445-1458.

1127Veres, D., Bazin, L., Landais, A., Kele, H.T.M., Lemieux-Dudon, B., Parrenin, F., Martinerie, P., Blayo, E.,  
1128Blunier, T., Capron, E., Chappellaz, J., Rasmussen, S.O., Severi, M., Svensson, A., Vinther, B. and Wolff,  
1129E.W. (2013) The Antarctic ice core chronology (AICC2012): an optimized multi-parameter and multi-site  
1130dating approach for the last 120 thousand years. *Climate of the Past*, **9**, 1733-1748.

1131Verheyden, S. (2012) The 8.2 ka event: is it registered in Belgian speleothems? *Speleogenesis and*  
1132*Evolution of Karst Aquifers*, 3-8.

1133Verheyden, S., Baele, J.M., Keppens, E., Genty, D., Cattani, O., Hai, C., Edwards, L., Hucai, Z., Van  
1134Strijdonck, M. and Quinif, Y. (2006) The proserpine stalagmite (Han-sur-Lesse cave, Belgium):  
1135Preliminary environmental interpretation of the last 1000 years as recorded in a layered speleothem.  
1136*Geologica Belgica*, **9**, 245-256.

1137Verheyden, S., Genty, D., Deflandre, G., Quinif, Y. and Keppens, E. (2008) Monitoring climatological,  
1138hydrological and geochemical parameters in the Pere Noel cave (Belgium): implication for the  
1139interpretation of speleothem isotopic and geochemical time-series. *International Journal of Speleology*,  
1140**37**, 221-234.

1141Verheyden, S., Keppens, E., Fairchild, I.J., McDermott, F. and Weis, D. (2000) Mg, Sr and Sr isotope  
1142geochemistry of a Belgian Holocene speleothem: implications for paleoclimate reconstructions.  
1143*Chemical Geology*, **169**, 131-144.

1144Verheyden, S., Keppens, E., Quinif, Y., Cheng, H.J. and Edwards, L.R. (2014) Late-glacial and Holocene  
1145climate reconstruction as inferred from a stalagmite - Grotte du Pere Noel, Han-sur-Lesse, Belgium.  
1146*Geologica Belgica*, **17**, 83-89.

1147Woillard, G.M. (1978) Grande Pile peat bog: A continuous pollen record for the last 140,000 years.  
1148*Quaternary Research*, **9**, 1-21.

1149Wolff, E.W., Chappellaz, J., Blunier, T., Rasmussen, S.O. and Svensson, A. (2010) Millennial-scale  
1150variability during the last glacial: The ice core record. *Quaternary Science Reviews*, **29**, 2828-2838.

1151Wynn, P.M., Fairchild, I.J., Spotl, C., Hartland, A., Matthey, D., Fayard, B. and Cotte, M. (2014)  
1152Synchrotron X-ray distinction of seasonal hydrological and temperature patterns in speleothem  
1153carbonate. *Environmental Chemistry*, **11**, 28-36.

1154Zhuravleva, A., Bauch, H.A. and Van Nieuwenhove, N. (2017) Last Interglacial (MIS5e) hydrographic  
1155shifts linked to meltwater discharges from the East Greenland margin. *Quaternary Science Reviews*, **164**,  
115695-109.